nature neuroscience

Article

https://doi.org/10.1038/s41593-026-02332-x

Tryptamine from wake-active monoaminergic neurons regulates sleep homeostasis

Received: 8 February 2025

Accepted: 7 May 2026

Published online: 19 June 2026

Check for updates

Huateng Cao (曹华腾)[1,2], Kui Wang (王逵)[1], Jin Zhao (赵津)[1,3], Zhong-Hua Zha (查中华)[4,5], Qian Zhang (张倩)[1], Yijin Xiu (修奕津)[1,3], Bangsheng Wu (吴邦胜)[6], Shajin Huang (黄沙金)[1], Xiao-Na Zhu (朱晓娜)[7], Xiaoting Li (李潇婷)[4], Jianan Chen (陈家楠)[8], Han Wen (温翰)[9], Siwen Pan (潘思文)[1,3], Ke-Xin Yang (杨可心)[5], Ji Hu (胡霁)[5], Jin-tai Yu (郁金泰)[6], Zhi-Jie Liu (刘志杰)[4,5], Tian Hua (华甜)[4,5], Yu Mu (穆宇)[1] ✉, Zhian Hu (胡志安)[10,11] ✉, Peng Yuan (袁鹏)[12] ✉ & Zhe Zhang (张哲)[1] ✉

Wakefulness produces sleep-promoting substances and the cerebrospinal fluid contains substances that reflect homeostatic sleep pressure. However, identities of such molecules, and the neural mechanisms for producing and sensing them, remain mysterious. Here we show that cerebrospinal fluid levels of tryptamine (TrpA) track homeostatic sleep pressure in nocturnal mice and diurnal pigs, reflecting physical activity history independently of light–dark cycles. We developed a ratiometric fluorescent sensor for TrpA and showed that TrpA is produced by wake-active monoaminergic nuclei in the diencephalon and brainstem and is secreted in an activity-dependent manner. We showed that released TrpA binds to G-protein-coupled receptor 139 (GPR139) and enhances neuronal excitability in the hypothalamic preoptic area to promote sleep. TrpA–GPR139 signaling was necessary for homeostatic sleep rebound and small-molecule GPR139 agonists promoted sleep duration and quality. Together, our study reveals TrpA as a signal related to sleep homeostasis and GPR139 as a druggable target against its disruption.

Sleep pressure is a driving force for sleep that accumulates during wakefulness and dissipates during sleep[1]. Its disruption is a common feature in sleep disorders, in which extended wakefulness cannot induce effective recovery sleep[2–4]. Earlier studies demonstrated that constituents of cerebrospinal fluid (CSF) contain signaling molecules for sleep homeostasis[5–7]. Despite keen interests in searching for these molecules for over a century[5–9], their identity remains mysterious[10,11]. Several sleep-promoting molecules, such as adenosine, prostaglandin D_2 and nitric oxide, have been discovered in the brain[10,11]. However, their production may not reflect wake-specific neural activity and studies found that eliminating the related receptors in the brain did not affect physiological sleep[12–14]. Thus, the endogenous molecules that promote sleep are still not fully understood.

How does extended wakefulness promote sleep? A potential mechanism is that wake-specific brain activities may generate sleep pressure[10,11,15]. For example, monoaminergic neurons are predominantly wake active and they produce neuromodulators with crucial functions for cognition and emotion[10,16]. These neurons are ideally positioned as generators for sleep pressure if they produce a sleep-promoting molecule as a side product of their functions. Previous study has not identified such molecules and the mechanism underlying wakefulness-induced sleep pressure remains elusive.

A full list of affiliations appears at the end of the paper. ✉e-mail: my@ion.ac.cn; zhianhu@aliyun.com; pyuan@fudan.edu.cn; zhezhang@ion.ac.cn

In our present study, we used targeted mass spectrometry (MS) and liquid chromatography to analyze the neuromodulators in CSF and discovered that the levels of tryptamine (TrpA) correlate with sleep pressure in nocturnal mice and diurnal pigs. We further combined single-cell transcriptome, new TrpA sensors, structural biology, in vivo optogenetics and pharmacology to dissect the neuronal source and effector of TrpA. Notably, we found that wake-active monoaminergic neurons produce TrpA in an activity-dependent manner, as an intermediate metabolite for producing neuromodulators and TrpA excites sleep-promoting hypothalamic neurons via G-protein-coupled receptor 139 (GPR139). Our study demonstrates TrpA as an endogenous molecule for promoting sleep in the brain.

Results

CSF TrpA levels track homeostatic sleep pressure

Prior studies suggest that substances reflecting homeostatic sleep pressure are enriched in the CSF of sleep-deprived animals[5–7]. Identifying this substance will have profound implications for understanding the biological process that drives wake–sleep modulations. To search for it, we sampled mouse CSF at 6-h physiological sleep (low sleep pressure) and at 6-h sleep deprivation (SD; high sleep pressure) (Fig. 1a) and analyzed neurotransmitter and neuromodulator contents via targeted metabolomics (Fig. 1b). Differential analysis revealed an increase of a tryptophan metabolite, TrpA, in the SD group (Fig. 1c). To track CSF TrpA levels at different times of the day, we developed a quantitative method using ultra-high-performance liquid chromatography (UHPLC) and found that CSF TrpA accumulated during wake-dominant period (before zeitgeber time (ZT) 0 for mice) and dissipated during sleep-dominant period (after ZT0 for mice) (Fig. 1d). Importantly, when we performed a short sleep deprivation at ZT4, we observed an increase in CSF TrpA levels (Fig. 1e), indicating that TrpA levels change with sleep pressure.

To distinguish whether the observed effect was due to sleep pressure or the circadian cycle, we repeated these measurements from intrinsic period-shifted mice, which were housed in an all dark environment with activity recording by running wheels (Extended Data Fig. 1a). In these conditions, CSF TrpA levels also followed active and rest phases defined by running and showed increase after acute SD (Extended Data Fig. 1b). In addition, light stimulation in an all dark condition did not induce significant fluctuation in TrpA level (Extended Data Fig. 1b). These data indicated that TrpA did not reflect light–dark circadian cycles. Correlation analyses showed that TrpA levels were correlated with recent running wheel activities (Extended Data Fig. 1c,d), in line with the buildup of sleep pressure during wakefulness[17]. To examine whether SD-induced TrpA increase was due to stress, we measured the serum corticosterone levels in mice undergoing acute SD. We did not detect measurable differences compared to naive mice (Extended Data Fig. 1e), indicating that elevated TrpA was unlikely due to overall stress in mice.

As mice are nocturnal animals, we wondered whether TrpA dynamics in diurnal animals with similar sleep patterns to humans would also reflect homeostatic sleep pressure. To test this, we further measured CSF TrpA contents at different time points in miniature pigs (Fig. 1f). Again, we found that TrpA levels accumulated with wakefulness (ZT0–11 for pigs) and declined after sleep onset (ZT11–24 for pigs) (Fig. 1f). These data showed that, in both mice and pigs, the levels of TrpA in CSF tracked homeostatic sleep pressure.

To test whether CSF TrpA promotes sleep, we performed intracerebroventricular (i.c.v.) infusions of TrpA (Fig. 1g). Mice that received TrpA showed increased nonrapid eye movement (NREM) sleep compared with vehicle-infused mice in a dose-dependent manner (Fig. 1h,i and Extended Data Fig. 1f). In addition to prolonged total NREM time, individual NREM episode length and slow-wave activity in electroencephalography (EEG δ power) also increased acutely in mice receiving TrpA infusions (Fig. 1j), consistent with the expected phenotype from elevated sleep pressure[1]. In addition, we found consistent effects if TrpA was infused in the dark phase when sleep pressure was low in mice (Fig. 1k and Extended Data Fig. 1g). Notably, in mice receiving TrpA injections, the percentage of time spent in NREM sleep was higher in the light-phase group compared to the dark-phase one, suggesting an interaction between baseline (BL) sleep pressure and the sleep-promoting action of TrpA. To directly test this, we conducted TrpA infusions in three different sleep pressure conditions: BL, 2 h SD (SD2) and 4 h SD (SD4). We found that sleep duration in the vehicle group increased with longer sleep deprivation. TrpA infusion boosted sleep duration, but the effect plateaued with high sleep pressure (Extended Data Fig. 1h,i), suggesting that the effect of TrpA and sleep pressure may converge on the same downstream substrate. Together, these data demonstrated that TrpA is a sleep-promoting molecule in CSF and that TrpA levels closely track sleep pressure.

Wake-active monoaminergic neurons release TrpA during wakefulness. To further dissect the relationship between TrpA and sleep pressure, we next sought to understand the source of TrpA. Brain TrpA

Fig. 1 | TrpA is a homeostatic sleep substance in the CSF. a, Schematics of sleep pressure and somnogen levels in a dark-to-light (wake-to-sleep) cycle of typical (green) or SD (red) mice. **b**, Diagram for CSF collection and targeted metabolomics. **c**, Quantification of the CSF molecules in normalized levels (pooled sample from eight (SD6 group) and five (S6 group) mice). **d**, Normalized (to ZT12) TrpA levels in mouse CSF from multiple ZTs measured by UHPLC. ZT12, ZT14, ZT0: $n = 7$ mice; ZT16, ZT20: $n = 8$ mice; ZT2, ZT4: $n = 10$ mice; ZT8: $n = 9$ mice; one-way analysis of variance (ANOVA) followed by multiple comparisons: P values: ZT0 versus ZT12, 0.0060; ZT0 versus ZT14, 0.0295; ZT0 versus ZT4, 0.0393; ZT0 versus ZT8, 0.0109. **e**, Normalized TrpA levels in mouse CSF from multiple time points in an SD + RS model (SD: ZT4–8; RS: ZT8–12), with comparison to the corresponding BL groups (dashed line in **e**, red dashed box in **d**). SD1: $n = 9$ mice; SD2: $n = 8$ mice; SD4, RS2, RS4: $n = 7$ mice; RS1: $n = 6$ mice; one-way ANOVA followed by multiple comparisons. P values: SD4 versus SD1, 0.0104; SD4 versus RS2, 0.0104; SD4 versus RS4, 0.0104; SD4 versus ZT4, 0.0104; SD4 versus ZT8, 0.0026; and SD4 versus ZT12, 0.0020. **f**, Schematic of the experiment and summary data of normalized (to ZT23) TrpA levels in pig CSF from multiple ZTs measured by UHPLC. ZT23, ZT13, ZT16: $n = 6$ mice; ZT2, ZT6: $n = 5$; one-way ANOVA followed by multiple comparisons. P values: ZT10 versus ZT23, 0.0058; ZT10 versus ZT2, 0.0133; ZT10 versus ZT13, 0.0283; and ZT10 versus ZT16, 0.0130. **g**, Schematics of i.c.v. cannular infusions of TrpA and sleep recordings. **h**, Examples of EEG spectrograms, electromyographic (EMG) traces and brain states from vehicle-treated and TrpA-treated free-moving mice. **i**, Cumulative percentages of brain states after vehicle and TrpA administrations ($n = 4$ mice per group, two paired infusions each mouse; two-way ANOVA followed by multiple comparisons (compare group means)). Top: light phase; bottom: dark phase. P values: vehicle versus TrpA (10 nmol), 0.0011; and vehicle versus TrpA (50 nmol), <0.0001. **j**, Quantitative data of NREM episode duration and EEG δ power in the first hour after vehicle and TrpA administrations ($n = 4$ mice per group, two paired infusions each mouse; Kruskal–Wallis test followed by multiple comparisons). Data are mean ± s.e.m., with lines connecting data from the same mouse. P values: vehicle versus TrpA (10 nmol), 0.0328 and vehicle versus TrpA (50 nmol), 0.0047 (left); vehicle versus TrpA (10 nmol), 0.0304 and vehicle versus TrpA (50 nmol), 0.0040 (right). **k**, Same as **g** and **i** but for TrpA administrations in the dark (active) phase ($n = 4$ mice per group, two paired infusions each mouse; two-way ANOVA, $P < 0.0001$). In this and all subsequent figures, each data point represents one mouse or a recording session and data are presented as the mean ± s.e.m., unless otherwise stated. P values are as indicated in the graphs: $^*P < 0.05$, $^{**}P < 0.01$, $^{***}P < 0.001$; all statistical tests were two-sided and the details of statistics are included in Methods. 5-HIAA, 5-hydroxyindole-3-acetic acid; 5-HTP, 5-hydroxytryptophan; Ach, acetylcholine chloride; DOPA, levodopa; Gln, L-glutamine; His, L-histidine; HisA, histamine; Kyn, DL-kynurenine; KynA, kynurenic acid; NE, noradrenaline; PA, picolinic acid; Trp, L-tryptophan; Tyr, L-tyrosine; freq., frequency; norm., normalized; REM, rapid eye movement; S6, 6-h in-sleep phase; SD6, 6-h sleep deprivation.

https://doi.org/10.1038/s41593-026-02332-x

is produced from tryptophan via decarboxylation by aromatic L-amino acid decarboxylase (AADC)[18] (Extended Data Fig. 2a). Intraperitoneal injection of an AADC inhibitor, NSD1015, blocked SD-induced TrpA rise in CSF (Extended Data Fig. 2b,c), indicating a necessary role for AADC in the production of TrpA in response to sleep pressure. In the brain, AADC is highly expressed in monoaminergic nuclei, including the locus coeruleus (LC), dorsal raphe (DR) and ventral tegmental area (VTA) (Extended Data Fig. 2d,e), because the same enzyme produces precursors for norepinephrine (NE), serotonin (5-hydroxytryptamine (5-HT)) and dopamine (DA)[18–20]. As monoaminergic neurons are known to be active during wakefulness and release neuromodulators[10,16], and brain TrpA is mainly associated with synaptosomes[21], we hypothesized that the monoaminergic system may contribute to brain TrpA production in an activity-dependent manner.

To directly monitor TrpA production in vivo, we engineered a genetically encoded, fluorescent ratiometric indicator for intracellular TrpA (TrpA sensor; Fig. 2a), by screening point mutations of our previously reported tryptophan sensor[22] (Extended Data Fig. 3a,b). We obtained a point mutation of Arg80Glu that showed selective response to TrpA, with minimal binding to tryptophan (Extended Data Fig. 3b). To further characterize its responses, we measured the fluorescence response to TrpA concentration gradients in purified proteins (Fig. 2b,c) or in *Escherichia coli* cells overexpressing this sensor (Fig. 2d,e) and found that micromolar-range TrpA elicited detectable response, which was one order of magnitude more sensitive than tryptophan (Fig. 2b). Metabolites with similar structures such as 5-HT and phenylalanine did not cause a fluorescence response (Fig. 2b,d), indicating that the Arg80Glu mutant can be a selective TrpA sensor. Another Arg54Gly mutation completely abolished the response to TrpA, which we used as a silent control (mutant sensor, Fig. 2b,e). We further measured the binding kinetics between TrpA and the sensor, which showed apparent association (k_{on}) and dissociation (k_{off}) rate

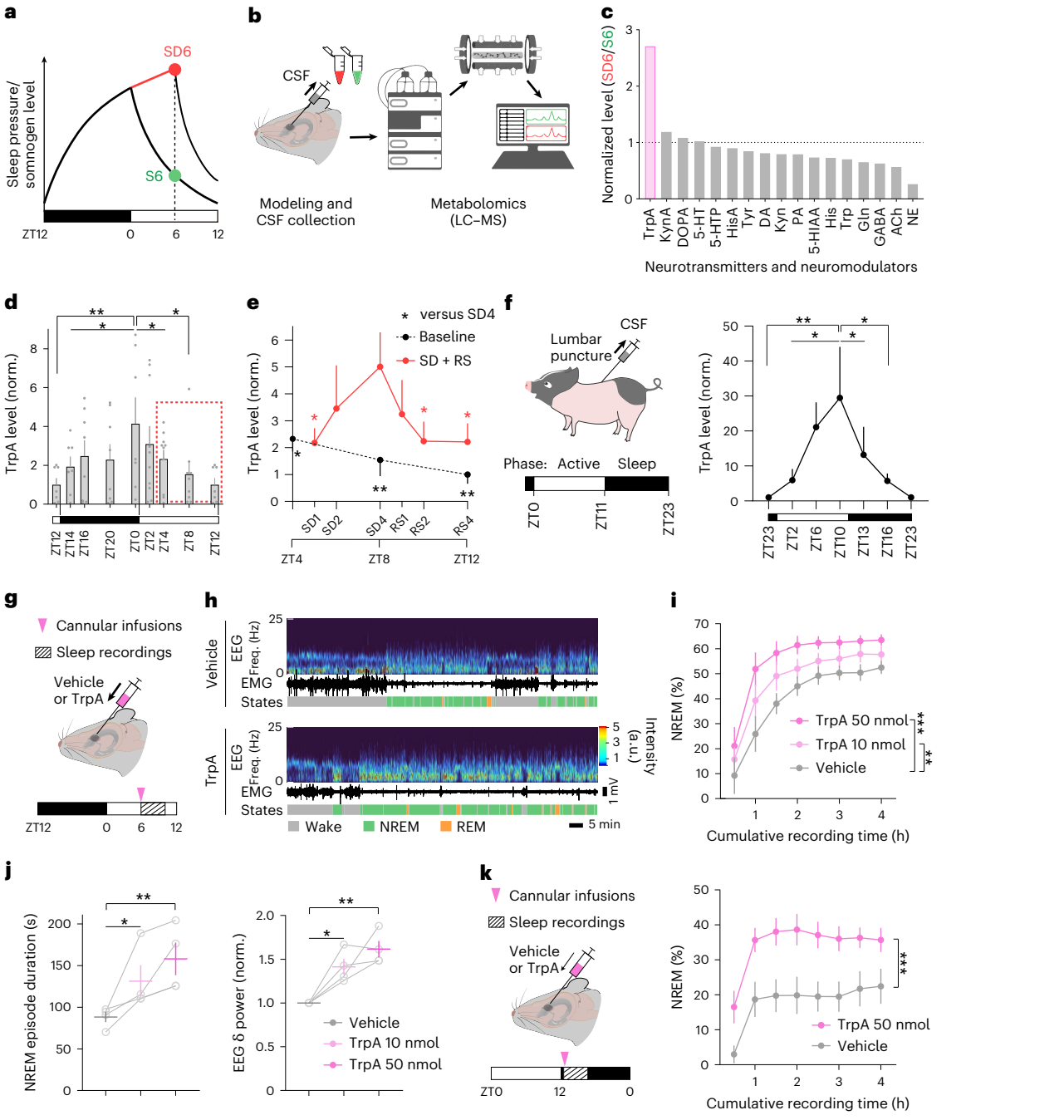

https://doi.org/10.1038/s41593-026-02332-x

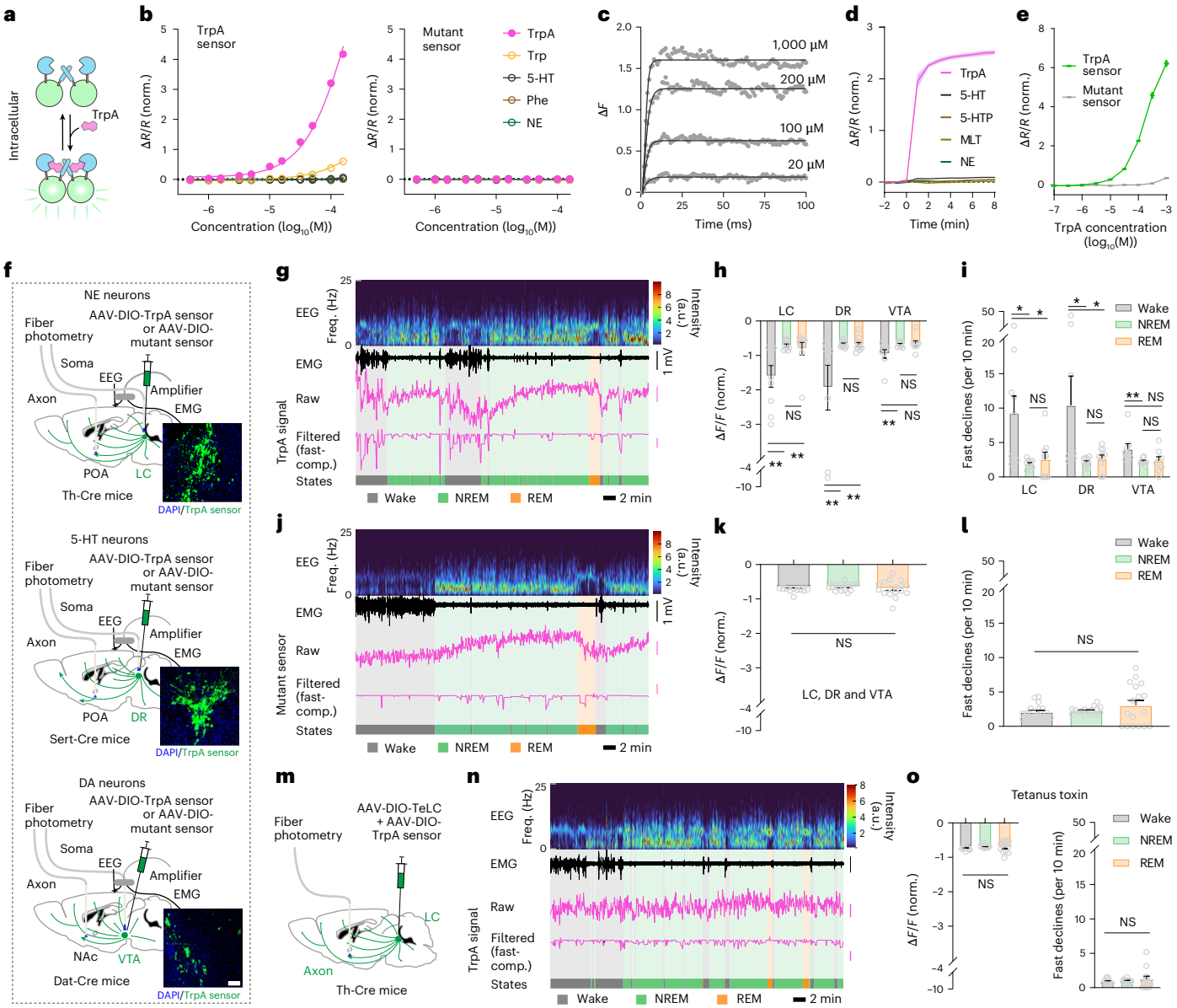

Fig. 2 | Monoaminergic neurons release TrpA during wakefulness. a, Schematic for the working mechanism of the TrpA sensor, which is composed of a mutant TrpR (cyan) and a cpSFYFP (green). TrpA (magenta) binding elicits fluorescence change. **b**, Excitation ratios of TrpA sensor (left) and silent mutant control (right) measured under varying concentrations of TrpA and related compounds in Hepes buffer ($n = 3$ independent experiments per group). **c**, Binding kinetics of TrpA sensor to TrpA measured using the stopped-flow technique in Hepes buffer. The data were fitted by a monoexponential function at each concentration. The k_{on} and k_{off} rate constants were 0.55 $\mu M^{-1} s^{-1}$ and 76.4 s^{-1}, respectively, resulting in a t_{on} of 0.018 s under 1 μM TrpA and a t_{off} of 0.013 s. **d**, The TrpA sensor specifically reacting to TrpA, but not other analogs in the brain. All drugs were added at a concentration of 100 μM ($n = 8$ independent experiments per group). **e**, Reactions of the TrpA sensor to a wide range of TrpA concentrations (1–1,000 μM) ($n = 8$ independent experiments per group). **f**, Schematics for fiber photometry recordings of TrpA sensor activity in soma and axonal regions of 5-HT neurons, NE neurons and DA neurons. Representative insets show infected neurons in the target regions. Scale bar: 100 μm. **g**, Representative data of simultaneously recorded EEG or EMG signals and TrpA sensor activity (LC axon). Scale bar: raw signal, 2 × s.d.; filtered signal, 5 × s.d. **h**,**i**, Quantitative data of TrpA sensor signal in the axon regions of monoaminergic neurons (LC^{Th}, DR^{Sert} and VTA^{Dat} neurons), shown as the averaged $\Delta F/F$ (**h**) and the fast declines of the signal (**i**), to demonstrate TrpA release. LC, $n = 9$ sessions; DR, $n = 10$ sessions; VTA, $n = 8$ sessions, ≥3 mice per group, Wilcoxon's matched-pair signed-rank test. *P* values in **h**: LC (awake versus NREM, 0.0078; awake versus REM, 0.0039; and NREM versus REM, 0.6523); DR (awake versus NREM, 0.0020; awake versus REM, 0.0098; and NREM versus REM, 0.4922); and VTA (awake versus NREM, 0.0078; awake versus REM, 0.1484; and NREM versus REM, 0.9453). *P* values in **i**: LC (awake versus NREM, 0.0195; awake versus REM, 0.0195; and NREM versus REM, 0.7344); DR (awake versus NREM, 0.0137; awake versus REM, 0.0371; and NREM versus REM, 0.4316); and VTA (awake versus NREM, 0.0078; awake versus REM, 0.1094; and NREM versus REM, >0.9999). **j**–**l**, Same as **g**–**i** but for the silent mutant control: 21 recordings (LC 12 + DR 5 + VTA 4) from 6 mice, Wilcoxon's matched-pair signed-rank test. **m**–**o**, Same as **g**–**i** but for TrpA signal in the axon terminals of NE neurons with TeLC expression: 12 recordings from 3 mice (4 recordings per mouse), Wilcoxon's matched-pair signed-rank test. Data are presented as the mean ± s.e.m.; all statistical tests were two-sided; *P* values are as indicated in the graphs: NS, not significant ($P > 0.1$); $^*P < 0.05$, $^{**}P < 0.01$. fast-comp., fast components; MLT, melatonin.

https://doi.org/10.1038/s41593-026-02332-x

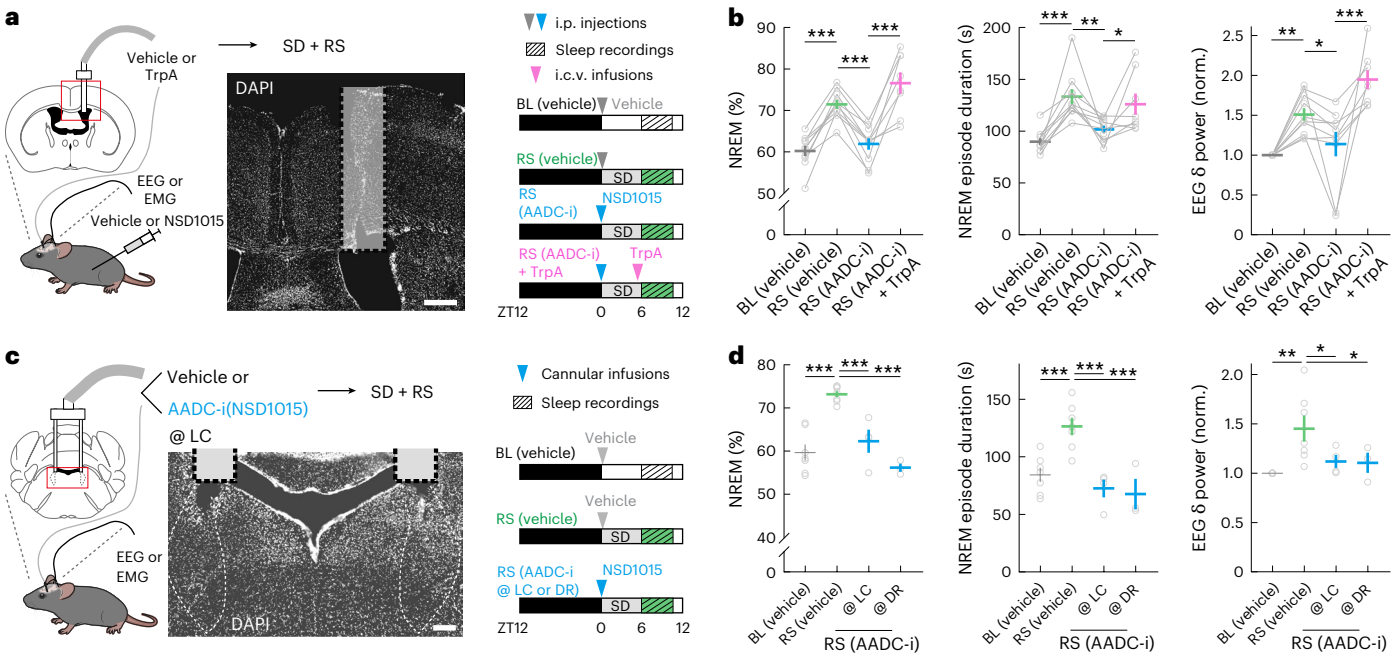

Fig. 3 | Production of TrpA in monoaminergic nuclei is required for homeostatic sleep rebound. a, Schematics and representative image of the brain tissue DAPI staining for the experiment of sleep rebound recordings under systematic AADC inhibitor (AADC-i) administrations or i.c.v. TrpA infusions. Scale bar, 200 µm. **b**, Quantitative data of sleep rebound recordings in **a** ($n = 10$ mice per group (except for RS (AADC-i) + TrpA: $n = 8$)). One-way ANOVA was used followed by multiple comparisons. *P* values are: all ≤0.0001 (left); RS (vehicle) versus BL (vehicle) <0.0001; RS (vehicle) versus RS (AADC-i) 0.0014; and RS (AADC-i) versus RS (AADC-i) + TrpA 0.0127 (middle); RS (vehicle) versus BL (vehicle) 0.0018; RS (vehicle) versus RS (AADC-i) 0.0145; and RS (AADC-i) versus RS (AADC-i) + TrpA <0.0001 (right). **c**,**d**, Same as **a** (**c**) and **b** (**d**) but for sleep rebound recordings with vehicle or AADC-i cannular infusions in LC or DR ($n = 4$ mice for LC group, $n = 3$ mice for DR group and $n = 7$ mice for vehicle group; one-way ANOVA followed by multiple comparisons). *P* values: RS (vehicle) versus BL (vehicle) or RS (AADC-i) at DR <0.0001; and RS (vehicle) versus RS (AADC-i) at LC 0.0004 (left); RS (vehicle) versus BL (vehicle) 0.0005; and RS (vehicle) versus RS (AADC-i) at LC or RS (AADC-i) at DR 0.0004 (middle); and RS (vehicle) versus BL (vehicle) 0.0048; and RS (vehicle) versus RS (AADC-i) at LC or RS (AADC-i) at DR 0.0406 (right). Scale bar, 200 µm. Data are presented as the mean ± s.e.m.; all statistical tests were two-sided; *P* values are as indicated in the graphs: $^*P < 0.05$, $^{**}P < 0.01$, $^{***}P < 0.001$. i.p., intraperitoneal.

constants as 0.55 $\mu M^{-1} s^{-1}$ and 76.4 s^{-1}, respectively (Fig. 2c). These data indicated a time on (t_{on}) of 0.018 s under 1 µM TrpA and time off (t_{off}) of 0.013 s, demonstrating that the sensor can reflect TrpA dynamics with centisecond time resolution.

We then expressed the sensor in mice via adeno-associated virus vectors and performed in vivo photometry measurements from the monoaminergic neurons in the LC, DR and VTA (LC^{Th}, DR^{Sert} and VTA^{DAT} neurons) (Fig. 2f and Supplementary Fig. 1) or other wake-promoting neurons in the paraventricular thalamus (PVT)[23] and tuberomammillary nucleus (TMN)[24]. We observed sharp downward fluctuations in the fluorescence signal from both axons and somata, particularly in monoaminergic neurons during awake periods (Fig. 2g–i and Extended Data Fig. 3c). These fast-decline events were absent in recordings using the inert mutant control (Fig. 2j–l and Extended Data Fig. 3d) and in recordings from nonmonoaminergic neurons in wake-active PVT and TMN nuclei (Extended Data Fig. 3e). These data suggested that the fast-decline events of the TrpA sensor may represent TrpA release from monoaminergic neurons. Consistent with this view, we found that the number of fast-decline events during wakefulness correlated with the EEG θ power (Extended Data Fig. 3f), an indicator for the intensity of wakefulness[10,25–27] and subsequent sleep homeostasis[28]. Activation of LC^{Th} or DR^{Sert} neurons caused decline of the intracellular TrpA sensor signal, at the same time leading to elevated levels of TrpA in the CSF, as measured by UHPLC (Extended Data Fig. 3g–i). Importantly, blocking synaptic release with the tetanus toxin light-chain (TeLC) virus abolished the wakefulness-enriched fast-decline events in monoaminergic neurons (Fig. 2m–o). Together, these data indicate that wake-active monoaminergic neurons produce and release TrpA in an activity-dependent manner, likely contributing to accumulation of TrpA with extended wakefulness.

We next tested whether elevated TrpA levels are causally linked to SD-induced sleep rebound. Consistent with the homeostatic effects of sleep pressure[1], mice exhibited sleep rebound after 6 h of SD, showing longer total NREM duration, extended individual NREM episodes and heightened δ power in EEG during the following recovery sleep (RS) (Fig. 3a,b). Systematic injection of NSD1015 blocked sleep rebound after SD and the effect was reversed when mice received i.c.v. infusion of TrpA (Fig. 3a,b). To locate the source of functionally relevant TrpA, we implanted microcannulae in the monoaminergic nuclei (LC, DR and VTA) and TMN and infused NSD1015 at the start of SD (Fig. 3c and Extended Data Fig. 4a). We found that suppressing the production of TrpA, both in LC and DR, abolished sleep rebound (Fig. 3d), whereas NSD1015 in VTA or TMN showed a weak or no effect (Extended Data Fig. 4b), respectively. Furthermore, chemogenetic inhibition of monoaminergic neurons in the LC and DR blocked SD-induced sleep rebound (Extended Data Fig. 4c,d), consistent with the activity-dependent release of TrpA from these regions. Our results show that TrpA is produced by wakefulness-related neural activities and regulates homeostatic sleep rebound, acting as a physical signal for sleep pressure.

Defined neurons in the POA express GPR139 that mediates the effect of TrpA. The above results established that TrpA in CSF tracks homeostatic sleep pressure; we next aimed to identify its downstream effector. We started by screening for TrpA-activated brain regions via measurement of the expression level of the immediate early gene (IEG) c-Fos in mice receiving i.c.v. infusions of TrpA. By comparison with

https://doi.org/10.1038/s41593-026-02332-x

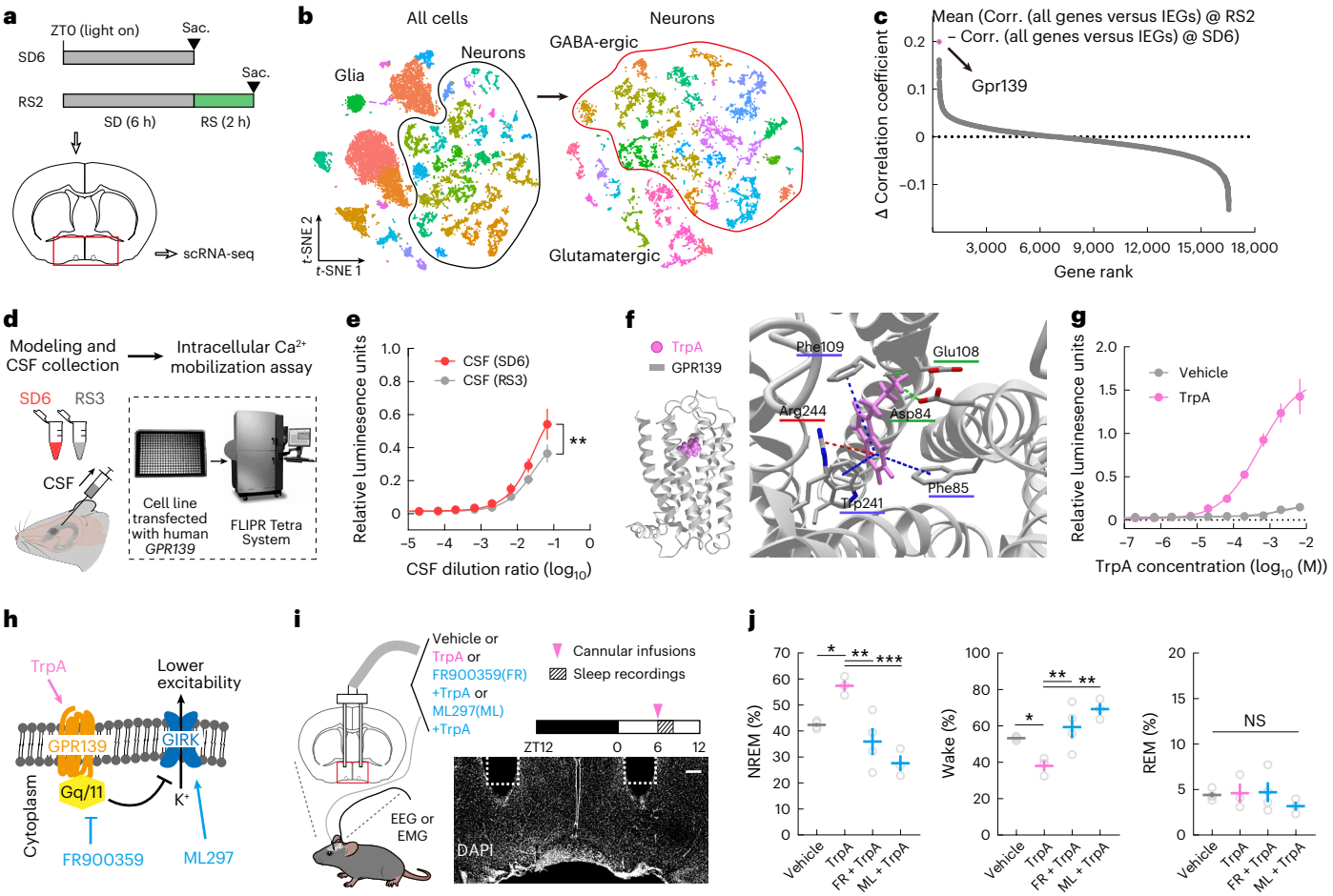

Fig. 4 | Identification of GPR139 in the POA as a receptor of TrpA. a, Schematic of brain tissue collection for scRNA-seq. **b**, Visualization of *t*-distributed stochastic neighbor embedding (*t*-SNE) of identified cell clusters from all cells (left) and neurons (right). **c**, Gene list ranked by the differential correlation coefficients with IEGs between RS2 and SD6 groups. **d**, Schematics of CSF collection and intracellular calcium mobilization assay. **e**, The calcium mobilization of GPR139 induced by CSF from SD6 and RS3 conditions ($n = 6$ independent experiments per group; two-way ANOVA, $P = 0.0056$). **f**, The docking pose of TrpA in GPR139. The TrpA is shown as magenta sticks and the key residues included in binding of GPR139 are shown as gray sticks. **g**, The calcium mobilization of GPR139 induced by TrpA or vehicle ($n = 6$ independent experiments for each group). **h**, Schematics of GPR139 signaling in neurons. **i**, Schematic and representative brain tissue DAPI staining image of cannular implantation in the POA. **j**, The percentages of brain states in 2 h after mice treated with TrpA alone or undergoing additional GPR139 signaling manipulations as shown in **i** ($n = 4$ mice in vehicle and TrpA + FR900359 groups; $n = 3$ mice in TrpA and TrpA + ML297 groups; one-way ANOVA followed by multiple comparisons). *P* values are: TrpA versus vehicle 0.0117; TrpA versus TrpA + FR 0.0020; and TrpA versus TrpA + ML 0.0006 (left); TrpA versus vehicle 0.0264; TrpA versus TrpA + FR, 0.0067; and TrpA versus TrpA + ML, 0.0016 (middle); TrpA versus vehicle 0.9853; TrpA versus TrpA + FR, 0.9853; and TrpA versus TrpA + ML, 0.8725 (right). Data are presented as the mean ± s.e.m.; all statistical tests were two-sided; *P* values are as indicated in the graphs: $^*P < 0.05$, $^{**}P < 0.01$, $^{***}P < 0.001$. Corr., correlation; FR, FR900359 (Gq inhibitor); ML, ML297 (GIRK activator); Sac., sacrifice.

mice receiving vehicle infusions, we found that the highest activation by TrpA occurred in the preoptic area of the hypothalamus (POA) (Supplementary Fig. 2), an area that has long been recognized as a center for sleep regulation[29–34]. We thus focused on the POA region for further investigations.

Next, we searched for the POA neurons associated with the sleep-promoting effect of TrpA. We hypothesized that these neurons are maximally activated during the initial RS after SD when the TrpA level is high. To this end, we performed single-cell RNA sequencing (scRNA-seq) of the POA region in mice with SD treatment and during the initial RS ($n = 4$ each) (Fig. 4a). We obtained a high depth dataset (total of 20,360 genes) of 17,118 qualified cells, out of which 8,543 were neurons (Fig. 4b and Supplementary Fig. 3). Unsupervised clustering yielded 41 neuronal subclusters (Extended Data Fig. 5a,b). We then compared the expression level of IEGs in each cluster of neurons in the SD and RS groups and found that a γ-aminobutyric acid (GABA)-ergic neuronal cluster (labeled 'i2') expressed high levels of IEGs, including *Fos*, *Egr1*, *Nr4a3* and so on, specifically in the RS condition (Extended Data Fig. 5c and Supplementary Fig. 4). Analysis of differentially expressed genes in the i2 cluster also indicated the presence of these IEGs (Extended Data Fig. 5d). These data suggest that POA i2 neurons could mediate the sleep-promoting effect of TrpA.

To further identify the molecular target expressed by POA i2 neurons that potentially respond to TrpA, we computed the covariance of each gene's expression levels with those of the IEGs for all cells. We assumed that high expression level of the TrpA molecular effector could lead to strengthened neuronal activation (IEG expression) and vice versa. When we ranked the genes by the magnitude of their correlation coefficients to the differential activation between the two groups, we found the top gene to be G-protein-coupled receptor 139 (*Gpr139*) (Fig. 4c). It is interesting that this gene was also a marker gene for neuronal cluster i2 (Extended Data Fig. 5c). Therefore, two independent analyses pointed to the same group of POA^{Gpr139} neurons as potential sleep-promoting responders to high levels of CSF TrpA.

Using a previously established intracellular calcium mobilization assay in a cell line transfected with human *GPR139*[35], we found that mouse CSF was also capable of activating GPR139-expressing cells and the CSF from SD mice induced heightened activation compared to that from RS mice (Fig. 4d,e). These data suggest that TrpA may directly interact with GPR139. GPR139 is a seven-transmembrane protein that has been implicated in schizophrenia[36,37]. We have previously resolved the structure of this protein[35] and its endogenous ligand is not known. With the solved structure, we then examined TrpA–GPR139 interaction with molecular docking. The docking results showed that TrpA binds to the orthosteric site of GPR139 and forms multiple hydrogen bonds and π-stacking interactions with GPR139 (Fig. 4f). Furthermore, using the same in vitro assay, we confirmed that TrpA potently activates GPR139 (Fig. 4g).

Previous studies showed that GPR139 activates the downstream G protein α subunit q/11 ($G_{q/11}$) pathway and inhibits G protein inward-rectifying potassium (GIRK) channels, thereby improving neuronal excitability[38] (Fig. 4h). To test whether the same molecular pathway underlies the sleep-promoting effect of TrpA, we performed pharmacological manipulations of the TrpA–GPR139 signaling via local microinfusions of the reagents in the POA (Fig. 4i). We found that bilateral infusion of TrpA in the POA promoted sleep and this sleep-promoting effect was blocked by co-administering a $G_{q/11}$ inhibitor (FR900359) or GIRK activator (ML297) (Fig. 4j). Together, these results indicated that TrpA activates a GPR139-mediated signaling pathway in the POA that promotes sleep.

POA^{Gpr139} neurons' excitability reflects homeostatic sleep pressure. The above results suggest that sleep homeostasis-related fluctuations of CSF TrpA levels modulate the excitability of POA^{Gpr139} neurons. To further test this, we generated a knock-in mouse model expressing *Cre*-recombinase with a hemagglutinin (HA) tag after the coding sequence of *Gpr139* (Gpr139-Cre; Fig. 5a). Using immunostaining in this mouse strain, we found that POA^{Gpr139} neurons were mainly located in the ventrolateral POA (VLPO) and the extended ventrolateral POA (extended VLPO) in the hypothalamus area (Extended Data Fig. 6a) and confirmed our sequencing data that POA^{Gpr139} neurons showed much higher c-Fos expression in RS compared to SD and S6–8 (free sleep) (Extended Data Fig. 6b).

We then directly measured the excitability of POA^{Gpr139} neurons in baseline sleep (S6) or sleep deprivation (SD6) conditions using patch-clamp electrophysiological recordings (Fig. 5b and Extended Data Fig. 6c). POA^{Gpr139} neurons from the SD group generated an action potential (AP) at a lower threshold (easier to fire; Fig. 5c,d) and produced more spikes under the same stimuli (Fig. 5e), indicating elevated neuronal excitability. Perfusing brain slices with exogenous TrpA also increased the excitability of POA^{Gpr139} neurons (Fig. 5f,g). These data provide direct evidence supporting the effect of TrpA in elevating the excitability of POA^{Gpr139} neurons.

We then investigated the in vivo activity profiles of POA^{Gpr139} neurons along the sleep–wake transitions. We injected AAV-DIO-GCaMP6s into the POA of Gpr139-Cre mice and performed fiber photometry calcium recording with polysomnographic recordings to detect the population neuronal activity and sleep–wake states simultaneously (Fig. 5h). We found that POA^{Gpr139} neurons showed strong activation during NREM and REM sleep and low activity in the awake state (Fig. 5i). Importantly, we observed that the degree of activity differences between NREM and awake (that is, sleep-specific activity) gradually diminished as the mice slept longer (Fig. 5i–k), consistent with reduced excitability of these neurons as sleep pressure dissipated. Consistently, averaged data from distinct sleep pressure conditions showed the same differences (Extended Data Fig. 7). In addition, we found that many POA^{Gpr139} neurons also express galanin (Supplementary Fig. 5a–d), a previously reported marker in the POA that is associated with sleep homeostasis[33,34]. Yet POA^{galanin} neurons consisted of multiple clusters[39,40]. As a group, they did not show sleep pressure-modulated activities (Supplementary Fig. 5e–h). Together, these results demonstrated that TrpA increases the excitability of POA^{Gpr139} neurons to encode sleep pressure in physiological as well as SD conditions.

Boosting TrpA–GPR139 signaling improves sleep homeostasis. We next investigated whether the activity of POA^{Gpr139} neurons is causally linked with sleep control. We injected Cre-dependent AAVs expressing optogenetic constructs in the POA of the Gpr139-Cre mice (Extended Data Fig. 8), which enabled us to manipulate the activities of POA^{Gpr139} neurons by light stimulation. We found that optogenetic inhibition led to robust transitions to the awake state, whereas optogenetic activation of POA^{Gpr139} neurons promoted NREM sleep (Extended Data Fig. 8). This is consistent with the projection of these inhibitory neurons to several wake-promoting brain regions (Extended Data Fig. 9). Thus, POA^{Gpr139} neurons are well positioned as a point for sleep control.

Based on the above results, it follows that the absence of TrpA–GPR139 signaling in the POA would disrupt sleep homeostasis. To directly test this, we utilized AAV-mediated CRISPR–Cas9 to knock out *Gpr139* gene locally in the POA (Fig. 6a and Extended Data Fig. 10a,b). Although i.c.v. infusion of TrpA induced sleep in control mice (Fig. 1g), deletion of the *Gpr139* gene in the POA abolished responses to TrpA (Fig. 6b,c), further confirming the necessity of this receptor in the POA for the sleep-promoting effect of TrpA. Consistently, mice receiving control viruses showed rebound sleep after sleep deprivation, as measured by increased total NREM duration, prolonged NREM episode length and elevated slow-wave activity (Fig. 6d,e). In addition, the POA *Gpr139* knockout (KO) mice showed fragmented and lighter sleep and failed to respond to SD treatment (Fig. 6d,e). Moreover, whole-brain *Gpr139* KO mediated by AAV-PHP.eB showed an effect on homeostatic sleep comparable to that of POA *Gpr139* KO (Extended Data Fig. 10c,d), validating the POA^{Gpr139} neurons as a necessary effector for homeostatic sleep. Taken together, in the 'flip-flop' framework[41] of sleep control, the TrpA–GPR139 signaling constitutes an ideal substrate for homeostatic sleep pressure (Fig. 6f).

Fig. 5 | TrpA modulates the excitability of POA^{Gpr139} neurons and encodes sleep pressure. a, Strategy for generating Gpr139-Cre mice. **b**, Schematic of the electrophysiological recording experiment. **c**–**e**, Representative electrophysiology recording traces and summary data of resting membrane potentials (**c**), AP thresholds (**d**) and spike frequencies (**e**) of POA^{Gpr139} neurons in the brain slices from mice with or without SD ($n = 32$ neurons in the S6 group and $n = 42$ neurons in the SD group; unpaired Student's t-test was used in **c** and **d**. P values are: 0.5170 in **c** and 0.0233 in **d**; two-way ANOVA in **e**, $P < 0.0001$. **f**,**g**, Representative traces and summary data of resting membrane potentials (**f**) and AP thresholds (**g**) of POA^{Gpr139} neurons in the brain slices with vehicle or TrpA incubation ($n = 15$ cells in the vehicle group; $n = 11$ cells in the TrpA group; unpaired Student's t-test; $P = 0.1473$ in **f** and $P = 0.0256$ in **g**. **h**, Schematics of fiber photometry experiment and representative image of GCaMP6s expression in POA^{Gpr139} neurons. Scale bar, 200 µm. **i**, Examples of EEG spectrogram, EEG δ power, EMG trace, calcium signaling and brain states in fiber photometry and EEG or EMG recordings. Scale bars, EMG, 1 mV; GCamP6s, 10% s.d. **j**,**k**, The z-scored calcium activity of POA^{Gpr139} neurons around NREM-to-wake transitions (**j**) and wake-to-NREM transitions (**k**). Heatmaps (left) show the calcium activity of individual transitions ranked by the recording time. Top right: the average calcium activity around transitions. Bottom right: average differences of calcium activity between mean 1 (before transition) and mean 2 (after transition) in different time slots of individual recording sessions. One-way ANOVA was followed by multiple comparisons ($n = 13$ recording sessions from 4 mice). P values in **j**: bin 1 versus bin 2, 0.0005; bin 1 versus bin 3, 0.0010; and bin 1 versus bin 4, <0.0001. P values in **k**: bin 1 versus bin 2, 0.0319; bin 1 versus bin 3, <0.0001; and bin 1 versus bin 4, <0.0001. Data are presented as the mean ± s.e.m.; all statistical tests were two-sided and P values are as indicated in the graphs: $^*P < 0.05$, $^{***}P < 0.001$. Rec., recording.

https://doi.org/10.1038/s41593-026-02332-x

It follows that boosting TrpA–GPR139 signaling may promote sleep. We first tested the effect of GPR139 agonists JNJ-63533054 (JNJ) and TAK-041 in vivo. As the agonists are capable of crossing the blood–brain barrier[37,42], we were able to achieve this treatment via systemic administration. We found that, compared to vehicle injections, JNJ or TAK-041 injections markedly promoted sleep duration and depth (Fig. 6g–i). Importantly, the effect in mice with *Gpr139* KO in POA did not respond to these treatments (Fig. 6g–i). These data indicated that boosting POA^{Gpr139} neuron excitability could promote sleep. This target is very likely relevant for human insomnia, because individuals with AADC deficiency exhibit sleep disturbance[43] and we found that genetic polymorphism of *GPR139* or *AADC* in humans is linked to elevated risks for sleep disorders (Supplementary Tables 1 and 2). Therefore, targeting TrpA–GPR139 signaling may be a new class of insomnia treatment.

Discussion

Our work discovered that TrpA was a previously unknown, endogenous sleep-promoting molecule in the brain. TrpA is an intermediate

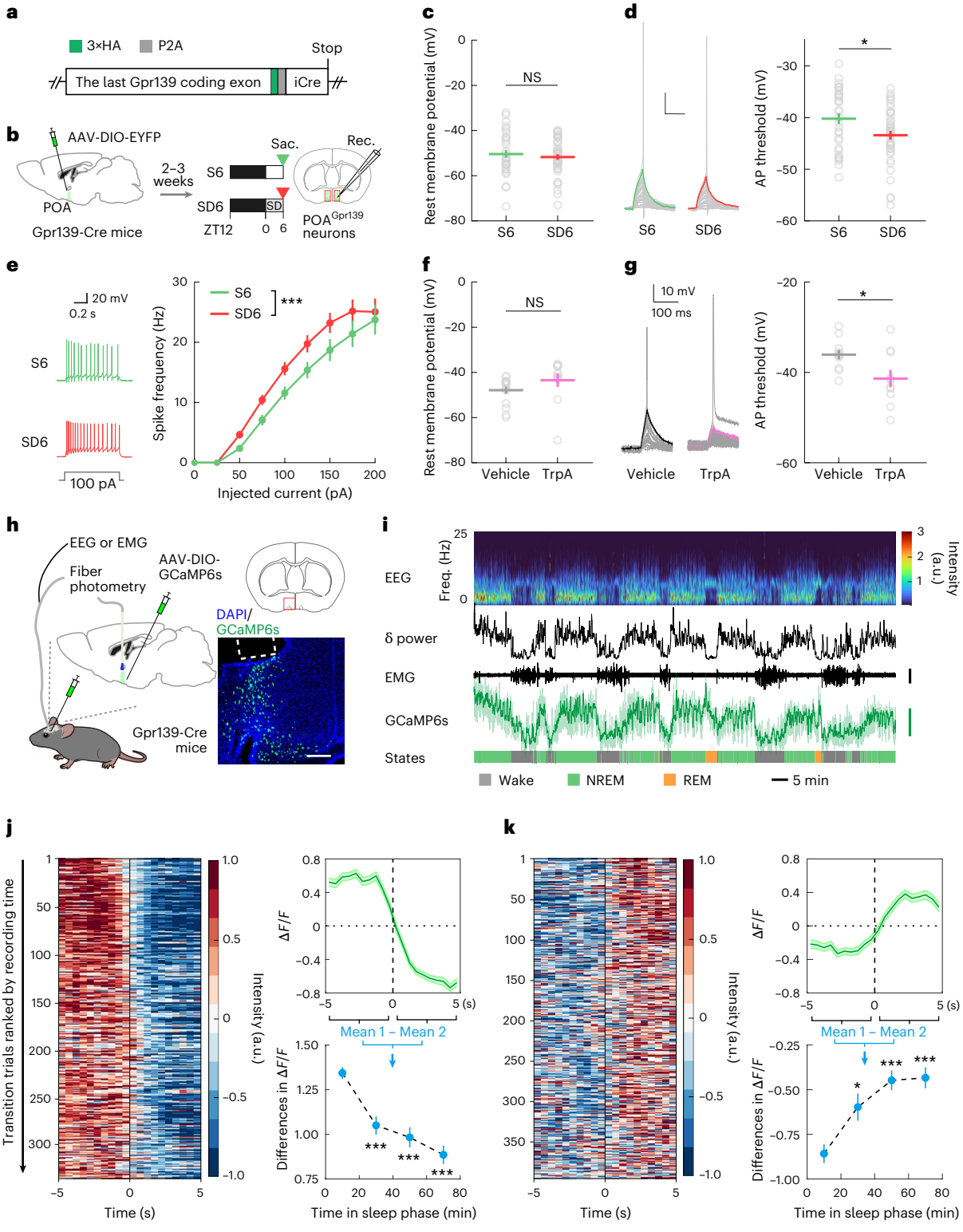

https://doi.org/10.1038/s41593-026-02332-x

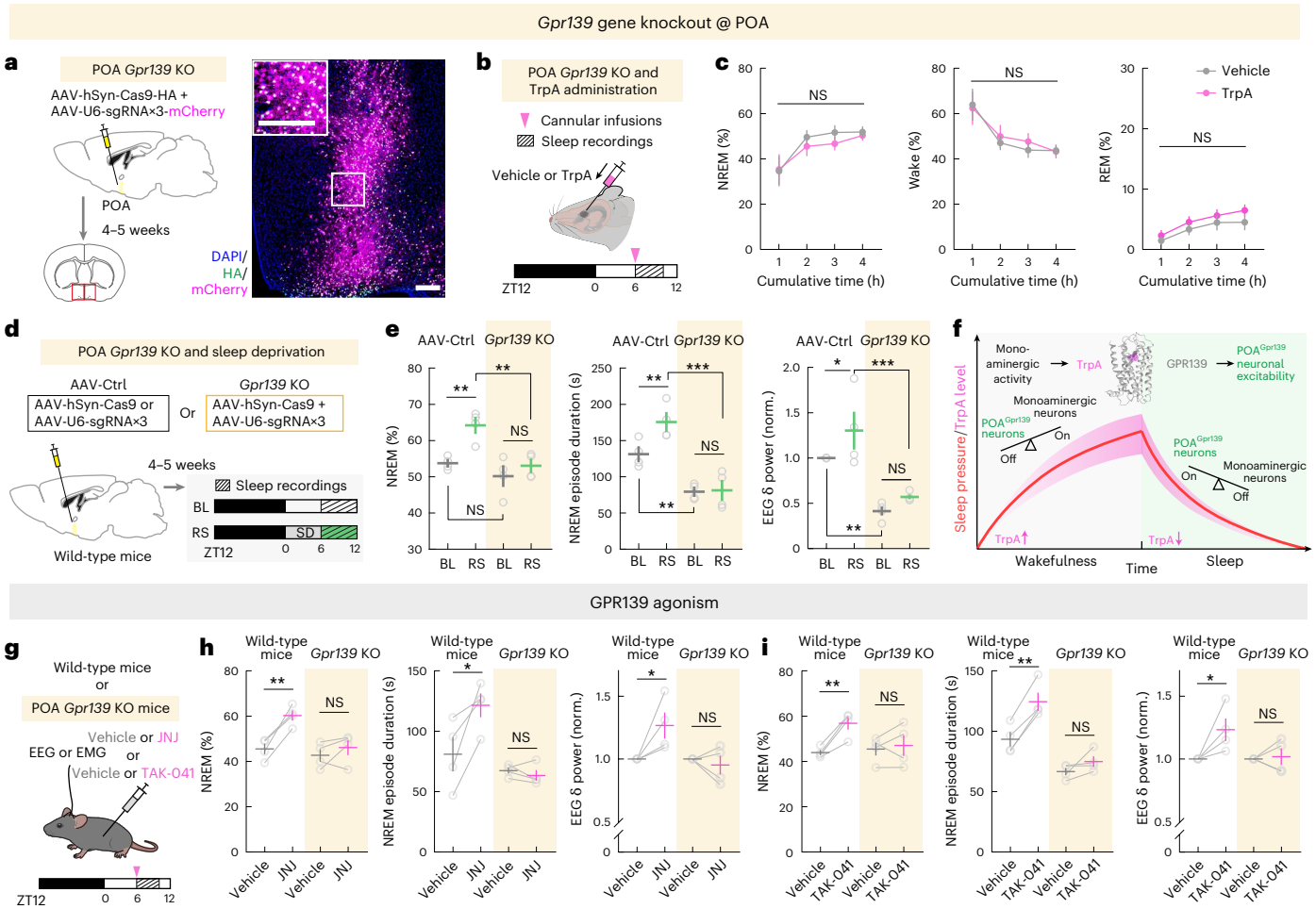

Fig. 6 | *Gpr139* signaling controls homeostatic sleep. a, Schematic of POA *Gpr139* KO using AAV-mediated CRISPR–Cas9 in the POA. Representative image of the infected neurons is shown in the POA. Scale bar, 200 µm. **b**,**c**, Schematics (**b**) and summary data (**c**) of cannular i.c.v. infusions of TrpA and sleep recordings ($n = 4$ mice per group; two-way ANOVA followed by multiple comparisons). **d**, Schematic of sleep recordings in BL and after sleep deprivation (RS) conditions of AAV-Ctrl or POA *Gpr139* KO mice. **e**, Quantification of sleep duration and depth indicated by total NREM sleep, NREM episode duration and EEG δ power in **d** ($n = 4$ mice per group; one-way ANOVA followed by multiple comparisons). *P* values are: BL versus RS, 0.0024 (control (Ctrl)) and 0.1989 (KO); BL versus BL, 0.1689; and RS versus RS, 0.0022 (left); BL versus RS, 0.0021 (Ctrl) and 0.1561 (KO); BL versus BL, 0.0013; and RS versus RS, <0.0001 (middle); and BL versus RS, 0.0300 (Ctrl) and 0.1150 (KO); BL versus BL, 0.0017; and RS versus RS, 0.0005 (right). **f**, Diagram representing sleep pressure by TrpA–GPR139 signaling. The monoaminergic neurons are active during wakefulness and release TrpA, whereas TrpA regulates the excitability of POA^{Gpr139} neurons. This signal bridges the activity of wake-promoting nuclei to the excitability of sleep-promoting nuclei, constituting a physical substrate for sleep pressure. **g**, Schematics of vehicle and GPR139 agonist (JNJ or Tak-041) treatments and sleep recordings. **h**,**i**, The percentages of NREM sleep, NREM episode durations and slow-wave activities in 4 h after vehicle or GPR139 agonist (JNJ (**h**) or Tak-041 (**i**)) treatments ($n = 4$ mice per group, with each *n* representing averaged data from 2–3 pair recordings per mice; paired Student's *t*-test (percentage NREM and NREM episode duration) or Mann–Whitney *U*-test (EEG δ power)). *P* values are: in **h**: 0.0072 and 0.3430 (left); 0.0395 and 0.3863 (middle); and 0.0286 and >0.9999 (right); in **i**: 0.0098 and 0.6433 (left); 0.0028 and 0.2033 (middle); and 0.0286 and >0.9999 (right). The data are presented as the mean ± s.e.m.; all statistical tests were two-sided; *P* values are as indicated in the graphs: $^{*}P < 0.05$, $^{**}P < 0.01$, $^{***}P < 0.001$.

metabolite for producing monoamine neuromodulators. We demonstrated that monoaminergic nuclei secrete TrpA during awake periods and levels of CSF TrpA accumulate over prolonged wakefulness. High levels of TrpA in the CSF activate GPR139 signaling and enhance the excitability of the GPR139-expressing neurons in the POA. Activation of POA^{Gpr139} neurons suppresses downstream wake-promoting circuits and promotes sleep. During sleep, the secretion of TrpA from monoaminergic neurons is halted and CSF TrpA gradually dissipates, reducing sleep drive (Fig. 6f).

TrpA is different from previously identified sleep-promoting molecules[10–14], because the production of TrpA is specifically linked with wake-active monoaminergic neurons, suggesting that TrpA is an ideal substance bridging awake periods and sleep pressure. Importantly, our data are consistent with recent reports that monoaminergic nuclei are related to sleep pressure[44,45]. In addition, considering that elevated levels of monoamine modulators are associated with high saliency stimuli, the release of sleep-promoting TrpA from the monoaminergic system offers a potential explanation for increased sleep pressure after mental exertion[46]. Furthermore, TrpA and associated small molecules could constitute a set of signals for modulating brain states, for example, the precursor of TrpA, tryptophan, in the diet has been shown to modulate sleep[47]. Metabolites of TrpA, including serotonin and melatonin, are also known to regulate sleep[45,48,49]. Many small molecular psychedelics with a TrpA scaffold exhibit consciousness-altering effects[50,51], whereas their microdosing prompts NREM sleep[52–56]. The synthesis, metabolism and brain state-dependent release of TrpA in the brain remain to be examined in future studies.

Another important finding of our study is the identification of POA^{Gpr139} neurons as responders to elevated sleep pressure. GPR139 was previously identified as an orphan receptor. A few potential ligands,

including L-tryptophan, L-phenylalanine[57,58] and α-melanocyte-stimulating hormone[59], have been reported. The physiological or pathological function of GPR139 was not known. Although GPR139 is expressed by many brain regions, we found that the expression in the POA is important for the sleep-promoting effect of TrpA. On activation by TrpA, GPR139 recruits the downstream $G_{q/11}$ effector and suppresses GIRK channels, leading to a reduced threshold for the neurons to fire APs. The POA^{Gpr139} neurons are a group of inhibitory neurons that project to several brain regions known to contain wake-promoting neurons (Extended Data Fig. 8). It is likely that activation of POA^{Gpr139} neurons promotes sleep onset and maintenance by suppressing the wake-promoting circuits. Therefore, TrpA–GPR139 signaling is ideally positioned to regulate numerous wake-promoting or sleep-promoting nuclei[10,26,31,32,60,61] and to control sleep–wake transitions following flip-flop dynamics[62].

Several limitations of our study should be noted in interpreting our results. First, 24-h recordings showed that a single TrpA infusion increased sleep duration and δ power for approximately 4 h but showed no change in the subsequent dark phase (Supplementary Fig. 6). Sleep deprivation, on the other hand, acutely induces sleep with elevated δ power and, in the subsequent dark phase, it induces more sleep but with reduced δ power[17]. Although the dynamics of recovery from sleep deprivation remain mechanistically complex[17] and injected TrpA was likely cleared in the dark phase, it is possible that responses to sleep deprivation involve different homeostatic mechanisms in different phases and TrpA does not modulate all aspects. Additional sleep homeostatic molecules likely exist and warrant future investigation. Second, we found that TrpA stimulates GPR139 at the tens of micromolar range (Fig. 4), yet the intracellular TrpA sensor did not allow direct measurement of TrpA release (Fig. 2). Therefore, although our data indicated TrpA–GPR139 signaling, other receptors or brain regions may be involved in mediating the effect of TrpA. Further studies are necessary to fully dissect the molecular mechanism underlying TrpA signaling.

Dysregulation of TrpA–GPR139 signaling could contribute to sleep disorders such as insomnia and boosting this signal may be a therapeutic target. A substantial proportion of patients with insomnia show reduced response to sleep pressure[2] and the effect of sleep restriction therapy is hard to sustain in the long-term[63]. Most current insomnia treatment focuses on suppressing neuron activity. It is interesting that a GPR139 agonist, JNJ-63533054, has recently been shown to promote sleep[64]. This target might be feasible to engage in the brain because another agonist, TAK-041, is currently under clinical trials for treatment for schizophrenia[37]. Identification of effective TrpA–GPR139 signaling activators that target homeostatic sleep regulation directly could represent a new and promising approach for insomnia therapy.

Online content

Any methods, additional references, Nature Portfolio reporting summaries, source data, extended data, supplementary information, acknowledgements, peer review information; details of author contributions and competing interests; and statements of data and code availability are available at https://doi.org/10.1038/s41593-026-02332-x.

References

1. Borbely, A. A. A two process model of sleep regulation. *Hum. Neurobiol.* **1**, 195–204 (1982).
2. Pigeon, W. R. & Perlis, M. L. Sleep homeostasis in primary insomnia. *Sleep Med. Rev.* **10**, 247–254 (2006).
3. Grimaldi, D. et al. Autonomic dysregulation and sleep homeostasis in insomnia. *Sleep* **44**, zsaa274 (2021).
4. Mander, B. A., Winer, J. R. & Walker, M. P. Sleep and human aging. *Neuron* **94**, 19–36 (2017).
5. Ishimori, K. True cause of sleep: a hypnogenic substance as evidenced in the brain of sleep-deprived animals. *Tokyo Igakkai Zasshi* **23**, 429–457 (1909).
6. Legendre, R. & Pieron, H. Recherche sur le besoin de sommeil consecutive a une veille prolongee. *Z. Allgem. Physiol.* **14**, 235 (1913).
7. Pappenheimer, J. R., Miller, T. B. & Goodrich, C. A. Sleep-promoting effects of cerebrospinal fluid from sleep-deprived goats. *Proc. Natl Acad. Sci. USA* **58**, 513–517 (1967).
8. Porkka-Heiskanen, T. et al. Adenosine: a mediator of the sleep-inducing effects of prolonged wakefulness. *Science* **276**, 1265–1268 (1997).
9. Sawada, T. et al. Prefrontal synaptic regulation of homeostatic sleep pressure revealed through synaptic chemogenetics. *Science* **385**, 1459–1465 (2024).
10. Eban-Rothschild, A., Appelbaum, L. & de Lecea, L. Neuronal mechanisms for sleep/wake regulation and modulatory drive. *Neuropsychopharmacology* **43**, 937–952 (2018).
11. Allada, R., Cirelli, C. & Sehgal, A. Molecular mechanisms of sleep homeostasis in flies and mammals. *Cold Spring Harb. Perspect. Biol.* **9**, a027730 (2017).
12. Stenberg, D. et al. Sleep and its homeostatic regulation in mice lacking the adenosine A1 receptor. *J. Sleep Res.* **12**, 283–290 (2003).
13. Huang, Z. L. et al. Adenosine A2A, but not A1, receptors mediate the arousal effect of caffeine. *Nat. Neurosci.* **8**, 858–859 (2005).
14. Urade, Y. et al. Sleep regulation in adenosine A2A receptor-deficient mice. *Neurology* **61**, S94–S96 (2003).
15. Krause, A. J. et al. The sleep-deprived human brain. *Nat. Rev. Neurosci.* **18**, 404–418 (2017).
16. Lorincz, M. L. & Adamantidis, A. R. Monoaminergic control of brain states and sensory processing: Existing knowledge and recent insights obtained with optogenetics. *Prog. Neurobiol.* **151**, 237–253 (2017).
17. Franken, P. & Dijk, D. J. Sleep and circadian rhythmicity as entangled processes serving homeostasis. *Nat. Rev. Neurosci.* **25**, 43–59 (2024).
18. Juorio, A. V. & Paterson, I. A. Tryptamine may couple dopaminergic and serotonergic transmission in the brain. *Gen. Pharmacol.* **21**, 613–616 (1990).
19. Marsden, C. A. & Curzon, G. Effects of lesions and drugs on brain tryptamine. *J. Neurochem.* **23**, 1171–1176 (1974).
20. Juorio, A. V., Greenshaw, A. J. & Nguyen, T. V. Effect of intranigral administration of 6-hydroxydopamine and 5,7-dihydroxytryptamine on rat brain tryptamine. *J. Neurochem.* **48**, 1346–1350 (1987).
21. Boulton, A. A. & Baker, G. B. The subcellular distribution of beta-phenylethylamine, *p*-tyramine and tryptamine in rat brain. *J. Neurochem.* **25**, 477–481 (1975).
22. Tao, R. et al. A genetically encoded ratiometric indicator for tryptophan. *Cell Discov.* **9**, 106 (2023).
23. Ren, S. et al. The paraventricular thalamus is a critical thalamic area for wakefulness. *Science* **362**, 429–434 (2018).
24. Yu, X. et al. Wakefulness is governed by GABA and histamine cotransmission. *Neuron* **87**, 164–178 (2015).
25. Rayan, A. et al. Sleep scoring in rodents: criteria, automatic approaches and outstanding issues. *Eur. J. Neurosci.* **59**, 526–553 (2024).
26. Scammell, T. E., Arrigoni, E. & Lipton, J. O. Neural circuitry of wakefulness and sleep. *Neuron* **93**, 747–765 (2017).
27. Bender, F. et al. Theta oscillations regulate the speed of locomotion via a hippocampus to lateral septum pathway. *Nat. Commun.* **6**, 8521 (2015).
28. Vyazovskiy, V. V. & Tobler, I. Theta activity in the waking EEG is a marker of sleep propensity in the rat. *Brain Res.* **1050**, 64–71 (2005).

29. Von Economo, C. Sleep as a problem of localization. *J. Nerv. Ment. Dis.* **71**, 249–259 (1930).
30. Nauta, W. J. Hypothalamic regulation of sleep in rats; an experimental study. *J. Neurophysiol.* **9**, 285–316 (1946).
31. Saper, C. B. & Fuller, P. M. Wake-sleep circuitry: an overview. *Curr. Opin. Neurobiol.* **44**, 186–192 (2017).
32. Liu, D. & Dan, Y. A motor theory of sleep-wake control: arousal-action circuit. *Annu. Rev. Neurosci.* **42**, 27–46 (2019).
33. Ma, Y. et al. Galanin neurons unite sleep homeostasis and alpha2-adrenergic sedation. *Curr. Biol.* **29**, 3315–3322 (2019).
34. Reichert, S., Pavon Arocas, O. & Rihel, J. The neuropeptide galanin is required for homeostatic rebound sleep following increased neuronal activity. *Neuron* **104**, 370–384 (2019).
35. Zhou, Y. et al. Molecular insights into ligand recognition and G protein coupling of the neuromodulatory orphan receptor GPR139. *Cell Res.* **32**, 210–213 (2022).
36. Dao, M., Stoveken, H. M., Cao, Y. & Martemyanov, K. A. The role of orphan receptor GPR139 in neuropsychiatric behavior. *Neuropsychopharmacology* **47**, 902–913 (2022).
37. Reichard, H. A. et al. Discovery of TAK-041: a potent and selective GPR139 agonist explored for the treatment of negative symptoms associated with schizophrenia. *J. Med. Chem.* **64**, 11527–11542 (2021).
38. Stoveken, H. M., Zucca, S., Masuho, I., Grill, B. & Martemyanov, K. A. The orphan receptor GPR139 signals via Gq/11 to oppose opioid effects. *J. Biol. Chem.* **295**, 10822–10830 (2020).
39. Moffitt, J. R. et al. Molecular, spatial, and functional single-cell profiling of the hypothalamic preoptic region. *Science* **362**, eaau5324 (2018).
40. Wu, Z., Autry, A. E., Bergan, J. F., Watabe-Uchida, M. & Dulac, C. G. Galanin neurons in the medial preoptic area govern parental behaviour. *Nature* **509**, 325–330 (2014).
41. Saper, C. B., Scammell, T. E. & Lu, J. Hypothalamic regulation of sleep and circadian rhythms. *Nature* **437**, 1257–1263 (2005).
42. Shoblock, J. R. et al. In vivo characterization of a selective, orally available, and brain penetrant small molecule GPR139 agonist. *Front. Pharmacol.* **10**, 273 (2019).
43. Pons, R. et al. Aromatic L-amino acid decarboxylase deficiency: clinical features, treatment, and prognosis. *Neurology* **62**, 1058–1065 (2004).
44. Silverman, D. et al. Activation of locus coeruleus noradrenergic neurons rapidly drives homeostatic sleep pressure. *Sci. Adv.* **11**, eadq0651 (2025).
45. Oikonomou, G. et al. The serotonergic raphe promote sleep in zebrafish and mice. *Neuron* **103**, 686–701 (2019).
46. Goldstein, C. A. & Chervin, R. D. in *Disorders of Sleep and Circadian Rhythms in Parkinson's Disease Regulation of Sleep and Wake Homeostasis* (eds Videnovic, A. & Högl, B.) 3–18 (Springer Vienna, 2015).
47. Binks, H., Vincent, G. E., Gupta, C., Irwin, C. & Khalesi, S. Effects of diet on sleep: a narrative review. *Nutrients* **12**, 936 (2020).
48. Monti, J. M. Serotonin control of sleep-wake behavior. *Sleep Med. Rev.* **15**, 269–281 (2011).
49. Zisapel, N. New perspectives on the role of melatonin in human sleep, circadian rhythms and their regulation. *Br. J. Pharmacol.* **175**, 3190–3199 (2018).
50. Fontanilla, D. et al. The hallucinogen *N*,*N*-dimethyltryptamine (DMT) is an endogenous sigma-1 receptor regulator. *Science* **323**, 934–937 (2009).
51. Araujo, A. M., Carvalho, F., Bastos Mde, L., Guedes de Pinho, P. & Carvalho, M. The hallucinogenic world of tryptamines: an updated review. *Arch. Toxicol.* **89**, 1151–1173 (2015).
52. Allen, N. et al. LSD increases sleep duration the night after microdosing. *Transl. Psychiatry* **14**, 191 (2024).
53. Rootman, J. M. et al. Adults who microdose psychedelics report health related motivations and lower levels of anxiety and depression compared to non-microdosers. *Sci. Rep.* **11**, 22479 (2021).
54. Anderson, T. et al. Psychedelic microdosing benefits and challenges: an empirical codebook. *Harm Reduct. J.* **16**, 43 (2019).
55. Barbanoj, M. J. et al. Daytime Ayahuasca administration modulates REM and slow-wave sleep in healthy volunteers. *Psychopharmacology* **196**, 315–326 (2008).
56. Murphy, R. J. et al. Acute mood-elevating properties of microdosed lysergic acid diethylamide in healthy volunteers: a home-administered randomized controlled trial. *Biol. Psychiatry* **94**, 511–521 (2023).
57. Isberg, V. et al. Computer-aided discovery of aromatic L-alpha-amino acids as agonists of the orphan G protein-coupled receptor GPR139. *J. Chem. Inf. Model.* **54**, 1553–1557 (2014).
58. Liu, C. et al. GPR139, an orphan receptor highly enriched in the habenula and septum, is activated by the essential amino acids L-tryptophan and L-phenylalanine. *Mol. Pharmacol.* **88**, 911–925 (2015).
59. Nohr, A. C. et al. The orphan G protein-coupled receptor GPR139 is activated by the peptides: adrenocorticotropic hormone (ACTH), alpha-, and beta-melanocyte stimulating hormone (alpha-MSH, and beta-MSH), and the conserved core motif HFRW. *Neurochem. Int.* **102**, 105–113 (2017).
60. Franks, N. P. & Wisden, W. The inescapable drive to sleep: overlapping mechanisms of sleep and sedation. *Science* **374**, 556–559 (2021).
61. Brown, R. E., Basheer, R., McKenna, J. T., Strecker, R. E. & McCarley, R. W. Control of sleep and wakefulness. *Physiol. Rev.* **92**, 1087–1187 (2012).
62. Saper, C. B., Fuller, P. M., Pedersen, N. P., Lu, J. & Scammell, T. E. Sleep state switching. *Neuron* **68**, 1023–1042 (2010).
63. Maurer, L. F., Schneider, J., Miller, C. B., Espie, C. A. & Kyle, S. D. The clinical effects of sleep restriction therapy for insomnia: a meta-analysis of randomised controlled trials. *Sleep Med. Rev.* **58**, 101493 (2021).
64. Wang, L. et al. Putative role of GPR139 on sleep modulation using pharmacological and genetic rodent models. *Eur. J. Pharmacol.* **882**, 173256 (2020).

[1]Institute of Neuroscience, CAS Center for Excellence in Brain Science and Intelligence Technology, Chinese Academy of Sciences, Shanghai, China. [2]Yiwu Research Institute of Fudan University, Yiwu, China. [3]University of Chinese Academy of Sciences, Beijing, China. [4]iHuman Institute, ShanghaiTech University, Shanghai, China. [5]School of Life Science and Technology, ShanghaiTech University, Shanghai, China. [6]Department of Neurology and National Center for Neurological Diseases, Huashan Hospital, State Key Laboratory of Medical Neurobiology and Ministry of Education Frontiers Center for Brain Science, Shanghai Medical College, Fudan University, Shanghai, China. [7]Shanghai Key Laboratory of Psychotic Disorders, Brain Health Institute, National Center for Mental Disorders, Shanghai Mental Health Center, Shanghai Jiao Tong University, School of Medicine and School of Psychology,

Shanghai, China. [8]DP Technology, Beijing, China. [9]AI for Science Institute, Beijing, China. [10]Department of Physiology, Institute of Brain and Intelligence, Third Military Medical University, Chongqing, China. [11]Chongqing Institute for Brain and Intelligence, Guangyang Bay Laboratory, Chongqing, China. [12]Department of Rehabilitation Medicine, Huashan Hospital, State Key Laboratory of Medical Neurobiology, Institute for Translational Brain Research, MOE Frontiers Center for Brain Science, MOE Innovative Center for New Drug Development of Immune Inflammatory Diseases, Fudan University, Shanghai, China. ✉e-mail: my@ion.ac.cn; zhianhu@aliyun.com; pyuan@fudan.edu.cn; zhezhang@ion.ac.cn

Methods

Animals

All animal procedures complied with the animal care standards set forth by the US National Institutes of Health (NIH) and were approved by the Animal Care and Use Committee of the Center for Excellence in Brain Science & Intelligence Technology, Chinese Academy of Sciences, Shanghai, China. Unless otherwise stated, mice were on a C57BL/6 background. Male and female mice were used for these experiments, aged 7–20 weeks and weighing 20–30 g. Mice were housed at 20–24 °C with 40–60% humidity and under a 12-h light to 12-h dark cycle, with food and water provided freely.

C57BL/6J mice were purchased from Shanghai Laboratory Animal Research Center. Gpr139-Cre mice were generated using CRISPR–Cas9-based technology by Biocytogen. The coding sequences of the HA tag (three repeats), P2A and Cre-recombinase were inserted into the end of the last exon (exon 2) of *Gpr139* guided by a single guide (sg)RNA (5′-AAGTATCCCCGTGACCCCACAGG-3′). Correct integration was confirmed by sequencing the PCR product and Southern blotting. Sert-Cre (B6.129(Cg)-*Slc6a4*$^{tm1(cre)Xz}$/J; RRID:IMSR_JAX:014554), Th-Cre (B6.Cg-*7630403G23Rik*$^{Tg(Th\text{-}cre)1Tmd}$/J; RRID:IMSR_JAX:008601), DAT-Cre (B6.SJL-*Slc6a3*$^{tm1.1(cre)Bkmn}$/J; RRID:IMSR_JAX:006660), Vglut2-Cre (stock *Slc17a6*$^{tm2(cre)Lowl}$/J; RRID:IMSR_JAX:016963) and Gad2-Cre (stock Gad2$^{tm2(cre)Zjh}$/J; RRID:IMSR_JAX:010802) mice were obtained from the Jackson Laboratory. Gal-Cre mice (stock Tg(Gal-cre)KI87Gsat/Mmucd, RRID: MMRRC 031060-UCD) were obtained from Mutant Mouse Resource & Research Centers.

Bama miniature pigs (female, aged 6–months) were purchased from and maintained at LenSci Limited, under an 11 h to 13 h light-to-dark cycle with food and water provided freely

Sleep deprivation

Sleep deprivation was carried out in a custom-made, closed-loop sleep recording and deprivation system, started at ZT0 and stopped at ZT6, mimicking a prolonged wake condition. Transistor–transistor logic signals were generated by a TDT recording system according to real-time recording and classification and sent to a self-developed Arduino-Stepping motor system, controlling a rotating bar at a suitable rotation speed. Once the mouse fell asleep, it would be mildly awakened by a rotating bar.

Polysomnographic recordings

A TDT recording system was used for polysomnographic recordings[65]. Electrode-implanted mice with their home cages were placed in soundproof, metal, recording boxes and their EEG and EMG electrodes were connected to a TDT RZ5 amplifier by flexible recording cables. All animals were handled in the recording environment for days before recordings. Recordings started after 30–60 min of habituation with headstage connection. EEG signals were recorded with bandpass filter 0.3–30 Hz and sampling rate of 610 Hz and were spectral analyzed using fast Fourier transform. EMG signals were recorded with a bandpass filter 10–200 Hz and sampling rate 610 Hz. The spectrum power of EEG and absolute EMG were used to classify brain states: NREM sleep (low EMG activity and synchronized EEG with high-amplitude and low-frequency (0.5–4.0 Hz) activity), REM sleep (low EMG activity and high power at θ frequencies (6–9 Hz)) and wake (high EMG activity and desynchronized EEG) states. The classification was determined semi-automatically using AccuSleep[66], an open-access graphic user interface programmed in MATLAB, followed by manual inspection.

CSF collection, metabolomics and UHPLC

CSF collections in mice were carried out from the lateral ventricles as previously reported[67]. Mice from SD6 (SD 5–6 h) and RS3 (SD + RS 3–4 h) groups were anesthetized with 1.0–1.5% isoflurane and fixed on a stereotaxic frame with level adjustment. CSF was collected from the lateral ventricles (anteroposterior (AnP) −0.22 mm, mediolateral (MeL) ±1.10 mm, dorsoventral (DV) −1.9 to −2.5 mm) at a speed of 10 nl s^{-1}. About 8–10 µl of CSF can be collected from a mouse. Lumbar puncture[68] was performed to collect CSF in six Bama miniature pigs every 4 h for a day.

Targeted metabolomics of neurotransmitters and neuromodulators were performed using an UHPLC coupled to tandem mass spectrometry (LC–MS/MS) system (ExionLC AD UHPLC-QTRAP 6500+ AB SCIEX Corp.) by Novogene. In brief, the samples were diluted twice and 100×. Then, 100 µl of the diluted sample was taken and homogenized with 300 µl of acetonitrile (80%) which contained mixed internal standards and centrifuged at 15,000*g* for 10 min. Finally, the supernatant (2 µl) was injected into the LC–MS/MS system for analysis. Separation was performed on a Waters XSelect HSS T3 column (2.1 × 150 mm^2, 2.5 µm) which was maintained at 45 °C. The mobile phase, consisting of 0.1% formic acid in 5 mM ammonium acetate (solvent A) and 0.1% formic acid in acetonitrile (solvent B), was delivered at a flow rate of 0.30 ml min^{-1}. The solvent gradient was set up as follows: initial 5% solvent B, 2 min; 5–40% solvent B, 4 min; 40–70% solvent B, 7 min; 70–100% solvent B, 7.5 min; 100% solvent B, 9 min; 100–5% solvent solvent B, 9.1 min; and 5% solvent B, 11 min. The mass spectrometer was operated in negative multiple reaction mode. Parameters were as follows: ion spray voltage (−4,500 V), curtain gas (241 kPa), ion source temperature (550 °C) and ion source gas of 1 and 2 (414 kPa). The ratio of the concentration of a standard to the internal standard as abscissa and the ratio of peak area of the standard to the internal standard as ordinate were used to investigate the linearity of the standard solution. The correlation coefficient (r) >0.99 of each metabolite was the necessary condition. The limit of quantification was determined using the method of signal-to-noise ratio, which compares the signal measured by the standard solution concentration with the blank matrix. Generally, when signal-to-noise ratio = 10:1, the corresponding concentration is the limit of quantification. Each group of CSFs for targeted metabolomics was from at least four mice.

The UHPLC-based TrpA concentration analysis was performed using a combined method: the Waters UHPLC Amino Acid Analysis Solution and UHPLC separation technology with AccQ·Tag Ultra Derivatization Chemistry (ACQUITY UPLC H-Class PLUS System, Waters). Samples were mixed with acetonitrile and centrifuged at 20,000*g* for 20 min. The supernatant was applied for further analysis. Automated, online, precolumn amino acid derivatization was performed by mixing *o*-phthalaldehyde and β-mercaptoethanol derivatizing reagent (2 µl) with the sample (0.5 µl) for 0.2 min before injection. The column (Eclipse Plus C18, 3.5 µm, 2.1 × 150 mm^2) was kept at 36 °C. The mobile phase consisted of solvent A (20 mM Na_2HPO_4 buffer, pH 6.8, 9% methanol and 5% acetonitrile) and solvent B (40% methanol and 40% acetonitrile). The flow rate of the mobile phase was 0.6 ml min. The concentrations were determined by ACQUITY H-Class Plus UPLC with FLR Detector (excitation wavelength 340 nm and emission wavelength 450 nm).

Development and validation of TrpA sensor

The TrpA sensor was derived from the previously reported tryptophan sensor GRIT[22]. GRIT consists of two domains: the recognition domain (TrpR) and the reporter domain (cpsfYFP). A point mutation was introduced into TrpR to enhance the GRIT sensor's response to TrpA while reducing its response to tryptophan. Briefly, molecular dynamics simulations were employed to model the TrpR–TrpA complex based on the crystal structure of TrpR–tryptophan. Within the complex, amino acid residues on TrpR that are near the TrpA molecule were identified. Considering the properties of these amino acids, beneficial mutations were hypothesized to enhance TrpA binding and weaken tryptophan binding. Favorable mutations were then introduced on TrpR of the GRIT sensor to construct candidate TrpA sensors. Then the candidate TrpA sensors were expressed in *E. coli* under the control of a T7 promoter and evaluated by adding TrpA and tryptophan solutions to live bacteria.

After screening about 100 mutations, the Arg80Glu mutation on TrpR substantially improved the sensor's response to TrpA while reducing its response to tryptophan. Therefore, GRIT (TrpR–Arg80Glu) served as the new TrpA sensor.

The cpYFP-based sensor is typically sensitive to pH and often requires the construction of a control sensor that does not respond to substrates to correct for pH effects[22,69]. In the published literature, introduction of the Arg54Gly mutation into TrpR has been shown to eliminate the sensor's response to tryptophan by reducing the binding between TrpR and the indole ring on tryptophan[22]. Molecular dynamics simulations indicated that the binding mode of TrpA with TrpR was similar to that of the TrpR–tryptophan complex and the Arg54Gly mutation also reduced the interaction between TrpR and the indole ring of TrpA. Experimental results in *E. coli* demonstrated that introduction of the Arg54Gly mutation effectively eliminates the sensor's response to TrpA. Therefore, GRIT–Arg54Gly served as the silent mutant control sensor for TrpA detection.

In vitro validation of the TrpA sensor was carried out using purified sensor protein. The biosensors were expressed in *E. coli* under the control of the T7 promoter. After overnight cultivation of *E. coli* monoclonal cells at 37 °C, induction of sensor expression was performed using isopropyl β-D-1-thiogalactopyranoside (0.1 mM) at 20 °C for 24 h. Bacteria were spun down at 4,000 rpm for 30 min at 4 °C. Cell pellets were suspended in protein purification binding buffer (30 mM sodium phosphate, 500 mM sodium chloride, 50 mM imidazole, 0.1 mg ml^{-1} of lysozyme, 0.1% Triton X-100 and 1 mM protease inhibitor cocktail, pH 7.4) and lysed with an ultrasonic cell disruptor (SCIENTZ Biotech). The supernatant was loaded on a nickel–nitrilotriacetic acid column (GE Healthcare) for affinity purification. The protein eluent was desalted in detection buffer (10 mM Hepes and 100 mM KCl, pH 7.3), quantified with a BCA kit (mxbioscience LLC). Then, 1 μM biosensors were used in a titration assay and stopped-flow kinetics assay. As a cpYFP-based excitation ratiometric sensor, the dual-channel signals of the TrpA sensor were detected to assess fluorescence changes, as previously reported[22]. In a titration assay, before and after adding the specified concentration of compounds, the dual-channel green fluorescence was read (excited at 485 nm with 12-nm bandpass filter and 420 with 12-nm bandpass filter, emitted at 520 nm) using a microplate reader (Varioskan LUX, Thermo Fisher Scientific) and the fluorescence ratio, $R_{488/420}$, calculated. Correction was conducted by dividing the fluorescence ratio ($R_{485/420}$) of the TrpA sensor by that of the control mutant sensor. The binding kinetics assay using a stopped-flow technique was performed with an SX20 Stopped-Flow accessory (Applied Photophysics Ltd). Due to the absence of a 420-nm excitation source in the SX20 system, only fluorescence changes excited at 488 nm were recorded. Briefly, 1 μM of protein solution was mixed 1:1 with TrpA of different concentrations (20, 100, 200 and 1,000 μM) and the fluorescence excited at 488 nm was measured with a 520 with 130-nm bandpass filter.

Viruses

Viruses for the expression of TrpA or mutant sensor and CRISR–Cas9 were packaged by the Gene Editing Facility of the Institute of Neuroscience (Shanghai, China), with the titers as follows: AAV-U6-sgRNA*3-mcherry (3.8×10^{13}), AAV-hSyn-Cas9-EGFP (7.3×10^{13}), AAV-hSyn-DIO-TrpA sensor (1.5×10^{14}) and AAV-hSyn-DIO-Mutant sensor (1.07×10^{14}). Other viruses were packaged by Shanghai Taitool Bioscience Co. Ltd with the following information: AAV2/8-hEF1a-DIO-eYFP-WPRE-PA (1.35×10^{13}, cat. no. S0196-8); AAV2/8-hSyn-FLEX-GCaMP6s-WPRE-pA (2.19×10^{13}, cat. no. S0026-8); AAV2/8-CAG-DIO-taCaspase3-TEVp-WPRE-pA (1.69×10^{13}, cat. no. S0236-8); AAV2/8-hEF1a-DIO-hChR2(H134R)-EYFP-WPRE-pA (1.47×10^{13}, cat. no. S0199-8); AAV2/9-hSyn-DIO-stGtACR2-eGFP-WPRE-pA (1.13×10^{13}, cat. no. S0625-9); AAV2/8-hEF1a-DIO-mCherry-P2A-TetTox-WPRE-pA (1.12×10^{13}, cat. no. S0506-8); AAV2/5-hsyn-DIO-hM3D(Gq)-mCherry-WPRE-pA (1.4×10^{13}, cat. no. S0192-5); AAV2/8-hSyn-DIO-hM4D(Gi)-mCherry-WPRE-pA (1×10^{13}, cat. no. S0193-8); AAV2/8-hSyn-hM3D(Gq)-ER2-P2A-mCherry-WPRE-pA (2.84×10^{13}, cat. no. S0487-8); AAV2/8-hSyn-hM4D(Gi)-ER2-P2A-mCherry-WPRE-pA (1.96×10^{13}, cat. no. S0498-8); and AAV2/8-hSyn-DIO-hChR2(H134R)-mCherry-ER2-WPRE-pA (1.33×10^{13}, cat. no. S0479-8).

Surgeries

Mice aged 7–9 weeks were anesthetized with 1.5% isoflurane and fixed on a stereotaxic frame with level adjustment. Level adjustment in the stereotaxic frame was conducted by equalizing the AnP axis (bregma and λ, DV heights <±0.05 mm) and MeL axis (bilateral points at bregma −1.5 mm and lateral to midline ±1.0 mm, DV heights <±0.05 mm). Erythromycin eye ointment was applied for eye protection and a heating pad was used to stabilize the mouse body temperature. The skull was exposed and a craniotomy was performed using a dental drill.

For EEG and EMG recordings, a reference electrode was connected to a screw inserted in the skull on top of the left cerebellum at AnP −6.2 mm and MeL −0.6 mm, two EEG electrodes were connected to screws inserted in the skull at AnP −3 mm and MeL ±2.6 mm and two EMG electrodes were inserted into the neck musculature. All electrodes were covered by insulative microtubes and soldered to a pin header.

For AAV-mediated TrpA or mutant sensor expression, viruses were injected into target regions at coordinates (DR: AnP −4.5 mm, MeL 0 mm, DV −3.1 mm; LC: AnP −5.4 mm, MeL ±0.9 mm, DV −3.6 mm; VTA: AnP −3.2 mm, MeL ±0.5 mm, DV −4.4 mm; PVT: AnP −1.2 mm, MeL 0 mm, DV −3.0 mm; and TMN: AnP −2.45 mm, MeL ±1.0 mm, DV −5.4 mm) using Nanoject III (Drummond Scientific) via micropipettes at a rate of 10 nl per cycle (10 nl s^{-1}) in 30-s intervals and a total volume of 150 nl (diluted). For other viral infections, viruses were injected into the target region of the POA at the coordinates (AnP, 0 mm; MeL, ±0.7 mm; DV, −5.25 to −5.65 mm) at a total volume (diluted) of 200 nl for AAV-DIO-GCaMP6s and AAV-DIO-taCasp3-TEVp, 50 nl for AAV-DIO-ChR2 and 100 nl for AAV-DIO-stGtACT2. All viruses, except for AAV-DIO-TrpA or mutant sensor and AAV-DIO-GCaMP6s, were injected bilaterally. Micropipettes were withdrawn 10–15 min after completion of the injection. AAV-PHP.eB expression in the whole brain was achieved by intravenous injections into the tail, a total of 2×10^{11} virus particles per mouse. For injections followed by optic fiber or cannula implantation, micropipettes were retained for longer (20–25 min) after injection completion. For optic fiber implantation in experiments of fiber photometry recordings or optogenetic manipulations, 400-μm or 200-μm diameter optic fibers were implanted into the target region with the tips 0.2 mm above the viral injection site. For cannular implantation, a customized single or bilateral cannula (RWD) was implanted into the lateral ventricle at AnP −0.22 mm, MeL ±1.1 mm and DV −2.4 mm or the POA at AnP 0 mm, MeL ±0.75 mm and DV −5.2 mm, respectively.

Light-curing adhesive (3M) was used to pre-fix the optic fiber and cannula immediately after implantation. Dental cement was applied to cover the skull and secure all elements on it.

Drugs and treatments

TrpA (tryptamine hydrochloride, MedChemExpress, cat. no. HY-W014971) was dissolved in 1× phosphate-buffered saline (PBS, pH 7.4, Sangon) at a concentration of 100 mM and aliquoted and stored at −80 °C before use. JNJ-63533054 (MedChemExpress, cat. no. HY-19838), TAK-041 (MedChemExpress, cat. no. HY-132228), NCRW0005-F05 (Axon Medchem, cat. no. Axon 2609) and ML297 (MedChemExpress, cat. no. HY-110192) were dissolved in dimethyl sulfoxide (DMSO) at a concentration of 50 mg ml^{-1} and aliquoted and stored at −80 °C before use. FR900359 (Cayman, cat. no. 33666) is a solution in acetonitrile at a concentration of 1.25 mM.

For cannular infusions, drug stocks were diluted into working concentration (NSD1015 30 μM, TrpA 5 mM, NCRW0005-F05 10 μM, ML297 30 μM and FR900359 10 μM) by 1× PBS, before use. For i.c.v. infusions, TrpA or vehicle (1× PBS) was cannular infused into free-moving mice using Nanoject III at a rate of 150 nl min^{-1} and a total volume of

1,000 nl per mouse. For cannular infusions in the LC, DR, VTA, PVT or TMN, vehicle or NSD1015 was infused into free-moving mice at a rate of 50 nl min^{-1} and a total volume of 200 nl per site (total 400 nl for bilateral infusions in LC, VTA or TMN). For cannular infusions in the POA, drugs or vehicles were bilaterally infused into the target brain regions (bilateral POAs) of mice under brief isoflurane anesthesia using Nanoject III at a rate of 20 nl per cycle (10 nl s^{-1}) in 30-s intervals and a total volume of 200 nl per site. The cannulas were kept for 5 min after completion of infusion and the mice were allowed to return to being wide awake for 1–2 min before polysomnographic recordings.

For intraperitoneal injections, GPR139 agonist (JNJ-63533054 or TAK-041) was diluted to a working concentration with a vehicle (corn oil) and injected at a dosage of 10 mg per kg (JNJ-63533054) or 5 mg per kg (TAK-041) body weight. Control injections (vehicle) were performed with the same volume of DMSO and corn oil.

Histology, immunohistology, FISH and imaging

Histology and immunohistochemistry were carried out as previously described[70,71]. Briefly, mice were anaesthetized with 0.14 g kg^{-1} of sodium pentobarbital and perfused with PBS, followed by ice-cold 4% phosphate-buffered paraformaldehyde (Sigma-Aldrich). Brains were dissected and post-fixed overnight in 4% paraformaldehyde, equilibrated in 30% sucrose at 4 °C and coronally sectioned at 30 µm. For immunohistochemistry, sections were preincubated in blocking solution 1 (5% bovine serum albumin (BSA; Sigma-Aldrich, cat. no. 9048-46-8) and 0.5% Triton X-100 in PBS) for 2 h at room temperature (RT). Primary antibody diluted in blocking solution 2 (3% BSA and 0.3% Triton X-100) was applied overnight at 4 °C. After rinsing in PBS, sections were incubated with secondary antibody in blocking solution 2 for 2 h at RT, followed by DAPI (Thermo Fisher Scientific, cat. no. D1306, RRID: AB_2629482, 1:3,000) staining for 15 min at RT. The primary antibodies and dilutions were: rabbit anti-DOPA decarboxylase (anti-AADC, Abcam, cat. no. ab3905, RRID: AB_304145, 1:500), chicken anti-tyrosine hydroxylase (anti-TH, Millipore, cat. no. AB9702, RRID:AB_570923, 1:500), rabbit anti-TPH2 (Abcam, cat. no. ab184505, RRID:AB_2892828, 1:500), rabbit anti-Fos (SynapticSystem, cat. no. 226008, RRID: AB_2891278, 1:600) and rat anti-HA (Roche, cat. no. 11867423001, RRID: AB_390918, 1:100). The secondary antibodies and dilutions were: donkey anti-rabbit Alexa Fluor-647 (Thermo Fisher Scientific, cat. no. A-31573, RRID: AB_2536183, 1:1,000), donkey anti-rat Alexa Fluor-488 (Thermo Fisher Scientific, cat. no. A-21208, RRID: AB_2535794, 1:1,000), goat anti-chicken Alexa Fluor-488 (Thermo Fisher Scientific, cat. no. A32931, RRID:AB_2762843, 1:1,000), goat anti-chicken Alexa Fluor-555 (Thermo Fisher Scientific, cat. no. A32932, RRID:AB_2762844, 1:1,000), donkey anti-rabbit Alexa Fluor-488 (Thermo Fisher Scientific, cat. no. A21206, RRID:AB_2535792, 1:1,000), donkey anti-rabbit Alexa Fluor-594 (Thermo Fisher Scientific, cat. no. A21207, RRID:AB_141637, 1:1,000), F(ab′)2-goat anti-rabbit immunoglobulin G (H+L) secondary antibody, FITC (Thermo Fisher Scientific, cat. no. 11-4839-81, RRID:AB_1210845, 1:300, for two-step staining of rabbit anti-DOPA decarboxylase and rabbit anti-TPH2). FISH was performed following the manufacturer's instruction of RNAscope Multiplex Fluorescent Assays v2 (Advanced Cell Diagnostics). The probes were Gpr139 (cat. no. 318051), iCre (cat. no. 423321-C2), Gal (cat. no. 400961-C3) and Fos (cat. no. 506931-C2). All sections were mounted in 75% glycerol. Images were acquired using a 65 Nikon C2 confocal microscope and a Plan Apo VC ×20 differential interference contrast objective (numerical aperture = 0.75) at 2-µm *z*-interval, except for the projection images, which were acquired using a fluorescence microscope (VS120, Olympus) and an UPlanSApo ×10 objective (numerical aperture = 0.4). Acquisition settings and thresholds were kept constant for each set of experiments. For example images, brightness or contrast adjustments within linear ranges were made using Fiji or ImageJ (NIH) across the entire image.

Quantitative analysis of histological images was performed using ImageJ. Cell numbers in different brain regions were counted automatically using a custom-made 'macro' with identical thresholds. Quantification of colocalization was performed manually using ImageJ (Extended Data Fig. 2 and Supplementary Fig. 4).

Fiber photometry recording and data processing

Fiber photometry was used to record the population-level intracellular TrpA level (TrpA or mutant sensor) and calcium signal (GCaMP)[72]. That was achieved using a Fiber Photometry Device RZ10x (Tucker-Davis Technologies) and a fluorescent port (Doric), which sent both 405-nm and 465-nm excitation lights to the participant and sensed the fluorophore responses at the same time. For excitation ratiometric TrpA or mutant sensor recordings, the excitation ratio (R) of the fluorescence signal was defined as the ratio of the 465-nm channel to the 405-nm channel (fitted) in fluorophore response. For GCaMP recordings, the fluorescence signal (F, 465-nm channel) was also divided by fitted isosbestic control signal (405-nm channel) to remove motion artifacts and photobleaching artifacts, as described previously[73]. The corrected F was used for further calculation. The $\Delta F/F$ was calculated (z-scored) as $(F - F_0)/F_{std}$, in which F_0 is the mean of F and F_{std} is the s.d. of F.

To identify and measure the fast components of TrpA or mutant sensor activity (sift out the activity more relevant to TrpA release and remove the slow drift), the $\Delta R/R$ was further processed using a MATLAB script 'BEADS' with a cut-off frequency of 0.09 cycles per sample (https://www.mathworks.com/matlabcentral/fileexchange/49974-beads-baselineestimation-and-denoising-with-sparsity) and normalized using the s.d. of activity during NREM sleep, as previously reported[74]. Then the fast signal was used to evaluate the activity of TrpA release, the number of fast declines (number of declines >3× s.d. every 2.5 s) indicating the frequency of TrpA release.

For state-coupling data analysis in each recording session, EEG spectrum powers were computed for every time bin (2.5 s per sleep or wake state bin) using the short-time Fourier transform. Wake-time bins were then ranked by their θ-band power and divided into ten equal groups (rank 1: 0–10%; rank 2: 10–20%; …; rank 10: 90–100%) within each session. For each rank group, the corresponding TrpA sensor activity—specifically, the rapid declines in the TrpA sensor signal indicative of TrpA release—was averaged across all time bins belonging to that group. These averaged values were used to generate the correlation plot (for example, Extended Data Fig. 3f).

Mice underwent fiber photometry recordings, accompanied by polysomnographic recordings, and underwent the same acclimation procedures as polysomnographic recordings. Each trial was recorded for >2 h. To minimize the bleaching effect of autofluorescence in the brain, we excluded the start of the recording data from further analysis in TrpA or mutant sensor recordings (12 min) and in GCaMP recordings (20 min).

ScRNA-seq and data processing

Act-seq[75] was applied to minimize the transcriptional changes during dissection for single-cell preparation with modifications. In brief, SD6 or RS2 mice were anesthetized with 0.7% sodium pentobarbital (0.14 g per kg body weight) and transcardially perfused with cold *N*-methyl-D-glucamine–artificial CSF (NMDG–aCSF), pH 7.3–7.4, osmotic pressure 300–310 mosmol containing (in mM): NMDG 90, KCl 2.5, $NaH_2PO_4 \cdot H_2O$ 1.2, $NaHCO_3$ 30, D-glutamic acid 25, Hepes 20, sodium ascorbate 5, thiourea 2, sodium pyruvate 3, *N*-acetylcysteine (NAC) 12, $MgSO_4$ 10 and $CaCl_2 \cdot 2H_2O$ 0.5. Coronal slices 330-µm thick were cut with a Leica VT 1200 s vibratome (Leica Microsystems). Brain slices were allowed to recover in a submerged chamber containing NMDG–aCSF for 8–12 min at 33 °C. Then the target POA regions were rapidly microdissected and cut into pieces under a dissecting microscope within 5 min and immediately transferred to aCSF (pH 7.3–7.4, osmotic pressure 300–310 mosmol, NaCl 126 mM, KCl 3 mM, $NaH_2PO_4 \cdot H_2O$ 1.2 mM, $MgCl_2 \cdot 6H_2O$ 1.3 mM, $CaCl_2 \cdot 2H_2O$ 2.4 mM, $NaHCO_3$ 26 mM and glucose 10 mM) dissolved in digestion solution (papain,

Worthington Kit). Digestion was carried out at 35.5 °C for 35 min with shaking of the tube every 5 min. Digested POA tissues were triturated by pipette tips, filtered by 40-µm filter (Thermo Fisher Scientific, cat. no. 352340) and washed and collected by gradient centrifugation (300*g*, 5 min) following the manufacturer's (Worthington Kit) instructions. To all the above solutions was added actinomycin D (10 µM, a transcriptional inhibitor; MedChemExpress) and oxygen was bubbled throughout all the procedures. Single cells were captured using 10x Chromium (10x Genomics) and libraries were prepared according the manufacturer's instructions (Chromium Next GEM Single Cell 3′-GEM, Library and Gel Bead Kit v3.1, 10x Genomics). Sequencing was performed on the Illumina NovaSeq 6000 system (paired end with read lengths of 150 nt, by Novogene).

Sequencing data were processed using Cell Ranger (10x Genomics)[76], in which the 'cellranger aggr' function was applied to normalize the sequencing depth of SD6 and RS2 conditions. Illumina sequencing reads were mapped to the mouse pre-mRNA reference transcriptome (mm10) with default parameters. The estimated number of cells is 18,368, the post-normalization mean reads per cell are 48,703 and the median genes per cell are 3,612. The normalized data were further analyzed using Seurat v4.0.4. Cells that met the following criteria were filtered out for downstream processing: (1) detected gene number: >200 and <9,000; (2) total unique molecular identifier counts <60,000; and (3) the percentage of mitochondrial genes <12%; 9,543 qualified cells in the SD6 group and 7,575 qualified cells in the RS2 group were used for further analysis. The 'logNormalize' (scale factor, 10,000) was used to normalize gene expression in each cell. The proportion of mitochondrial unique molecular identifiers was regressed out (ScaleData function). The top 2,000 variable genes were identified (FindVariableGenes function) and used as input for dimensionality reduction via principal component analysis after removal of interfering genes including sex-specific genes, IEGs, virus-induced genes and 1,000 noise-sensitive genes[77]. 'RunPCA' was applied to find the principal components (PCs) and 75 PCs were used as input for clustering analysis (FindClusters function, resolution = 0.6). Then, 36 clusters were identified and each cluster was classified to canonical cell types in the brain according to the following markers: Stmn2 for neurons, Cldn5 for endothelial cells, Aif1 for microglia, opalin for oligodendrocytes, Gja1 for astrocytes, Pdgfra for oligodendrocyte progenitor cells, Vtn for pericytes and Mustn1 for mural cells. Cells that belonged to neuronal clusters were applied to secondary clustering analysis using the above parameters, except for setting the resolution in FindClusters function as 1 instead. Forty-one clusters were identified and divided into two groups i and e: (i) GABA-ergic neuronal clusters expressing Slc32a1 and (e) glutamatergic neuronal clusters expressing Slc17a6. Then each cluster was assigned a specific name as group type (i or e) followed by a number indicating its location in the phylogenetic tree and one of the top marker genes (FindConservedMarkers function) of the cluster. FindMarkers functions were used to calculate the statistical differences of Fos between groups and identify the differentially expressed genes. The correlation coefficient was calculated using scaled data in Pearson's method.

Molecular docking

Molecular docking was performed using Schrödinger Suite 2022-3 to explore TrpA–GPR139 interactions. The TrpA-bound GPR139 was prepared using the Protein Preparation Wizard for optimized protonation and hydrogen bonding. Receptor grid generation was used to generate the grid. The two-dimensional (2D) structure of TrpA was obtained from PubChem and the conversion of TrpA from the 2D to the 3D structure was performed by 'LigPrep' processing, which included energy minimization and adjustment of ionization states at specific pH values using Epik[78,79]. The docking of TrpA to the GPR139 was conducted using a rigid protein-docking approach, employing the SP precision mode.

Intracellular calcium mobilization assay

CHO K1 cells (American Type Culture Collection, cat. no. CCL-61) were seeded at a density of 750,000 cells in 10-cm dishes overnight at 37 °C in F-12 (Gibco) supplemented with 10% fetal bovine serum and 1% penicillin–streptomycin solution. On the day of transfection, 1 µg of plasmid DNA from human GPR139 was transfected to the cells by TransIT2020 (Mirus Bio). After 24 h, cells were detached with 0.25% trypsin-EDTA (1×) solution (Gibco) and resuspended in F-12 supplemented with 10% fetal bovine serum and 1% penicillin–streptomycin solution. Cells were seeded in black-sided, clear-bottomed, 384-well plates (Agilent) at a density of 10,000 cells per 40 µl per well and incubated overnight at 37 °C and 5% CO_2. On the following day, growth medium was removed and cells were loaded with 20 µl per well of 1x FLIPR Calcium 6 dye (prepared in Hank's balanced salt solution (HBSS) buffer; Molecular Devices) and incubated for 1 h at 37 °C in the dark. JNJ-63533054 dilutions were prepared in HBSS with 1% BSA from 10 mM DMSO stocks whereas TrpA (MCE) dilutions were prepared from 200 mM HBSS stock solution. The CSF dilutions were prepared in HBSS with 1% BSA from collected mouse CSF (SD6 and RS3). The FLIPR was programmed to take 10 readings (1 read per second), initially as a baseline before the addition of 10 µl of 3× compound or CSF solution. The fluorescence intensity was recorded for 2 min for agonist activity detection. The relative luminescence unit was calculated by normalizing the relative fluorescence intensity (baseline intensity divided by fluorescence intensity, three repeats per concentration condition) to the last concentration condition (CSF 2×10^{-9} dilution, JNJ 1×10^{-11} M, TrpA: 2×10^{-9} M). Each group of data was from six to eight biological repeats.

Optogenetic manipulation

A 473-nm laser device (Shanghai Laser & Optics Century Co., Ltd, cat. no. ADR 700 A) was used to generate blue light for optogenetic activation of ChR2 or optogenetic inhibition of stGtACR2 under the control of a TDT system. Each trial consisted of 7–10 sessions lasting 120 s and a random interval between 15 min and 20 min. For optogenetic activation, the laser power was 1–2 mW at the fiber tip and the laser pulse was set as 20 ms at 5-Hz frequency. For optogenetic inhibition, the laser power was 3–4 mW at the fiber tip and the laser pulse was set as constant. Each animal was tested for three to six trials in the home cage during the light cycle.

Chemogenetic manipulation

Clozapine-*N*-oxide (Sigma-Aldrich, cat. no. C0832) dissolved in saline (0.9% NaCl) was applied to activate (1 mg per kg of body weight) or inhibit (3 mg per kg of body weight) neuron expression hM3D(Gq) or hM4D(Gi), respectively, by intraperitoneal injection. Saline was used in control injections.

Acute slice preparation and electrophysiological recording

Gpr139-Cre mice were injected bilaterally with AAV-DIO-eYFP in the POA and sacrificed 3–4 weeks later for acute slice preparation, without or with sleep deprivation (S6 or SD6).

Acute slice preparation was performed as previously reported[80]; mice were anesthetized with 0.7% sodium pentobarbital (0.14 g per kg body weight) and transcardially perfused with cold NMDG–aCSF (NMDG 93 mM, KCl 2.5 mM, $NaH_2PO_4 \cdot H_2O$ 1.2 mM, $NaHCO_3$ 30 mM, D-glutamic acid 25 mM, Hepes 20 mM, sodium ascorbate 5 mM, thiourea 2 mM, sodium pyruvate 3 mM, NAC 12 mM, $MgSO_4$ 10 mM and $CaCl_2 \cdot 2H_2O$ 0.5 mM, pH 7.3–7.4 and osmotic pressure 300–310 mosmol). Brains were removed and immersed in ice-cold NMDG–aCSF, then coronal slices 330-µm thick were cut with Leica VT 1200 s vibratome (Leica Microsystems). Brain slices were allowed to recover in a submerged chamber containing NMDG–aCSF for 10 min at 32 °C, followed by at least 1 h of recovery in aCSF (NaCl 126 mM, KCl 3 mM, $NaH_2PO_4 \cdot H_2O$ 1.2 mM, $MgCl_2 \cdot 6H_2O$ 1.3 mM, $CaCl_2 \cdot 2H_2O$ 2.4 mM, $NaHCO_3$ 26 mM and glucose 10 mM, pH 7.3–7.4 and osmotic pressure 300–310 mosmol) at

31 °C before recordings. Both NMDG–aCSF and aCSF were constantly bubbled with 95% O_2 and 5% CO_2.

For electrophysiological recording, individual slices were transferred to a recording chamber submersed in oxygen-bubbled aCSF at 26–30 °C. Target cells (EYFP-labeled neurons in the POA) were visualized and patch-clamped by glass pipettes (resistance, 3–5 MΩ), backfilled with internal solution (potassium gluconate 110 mM, KCl 20 mM, Hepes 20 mM, $MgCl_2$ 5 mM, (ethylenebis(oxonitrilo))tetra-acetate 0.6 mM, MgATP 2 mM and Na_3GTP 0.2 mM, pH 7.3, 290 mosmol). Recording was made using a Multiclamp 700B (Molecular Devices). The membrane resistance, membrane capacitance, series resistance and resting membrane potential were measured using Clampex Software. Resting membrane potential is recorded when '$I = 0$' immediately after cell break in. The cells were excluded if the series resistance exceeded 30 MΩ or varied by >20% during the recording period. The threshold of AP firing for each cell was carried out by measuring the highest potential of the trace that did not induce AP firing during a 25-ms depolarizing current injection of 2-pA increments in current-clamp mode. The excitability (spike frequency versus injected current) experiments were carried out by measuring the average AP firing rate during 800-ms depolarizing current injections of 25-pA increments in current-clamp mode. Each group of neurons (S6, 32; SD6, −42; vehicle for TrpA, 15; TrpA, 11) from at least three mice. All neurons were included in the statistical analyses and plotted in the figures, except for outliers of AP threshold and spike frequency that resulted from unstable responses under current injections, as indicated in the figure legends.

CRISPR–Cas9-mediated *Gpr139* KO

An optimized strategy as previously reported[81] was used for CRISPR–Cas9-mediated gene editing. In brief, three adjacent sgRNAs that targeted exon 2 of *Gpr139* were designed by CRISPOR (http://crispor.tefor.net)[82], the target sequences of which were as follows: 5′-TTACGGTCCCCTTAACGGTTG-3′, 5′-TTCCTACCCAGCCAGGACCCG-3′ and 5′-GAGGCATCTGCATGGTCAAAA-3′. Each sgRNA scaffold sequence was inserted after a U6 promoter. Three U6 promoter-based sgRNA elements were ligated together and cloned into an AAV construct for AAV-U6-sgRNA×3 packaging. KKH SaCas9 was subcloned into an AAV construct with a human synapsin 1 promoter for AAV-hSyn-Cas9 packaging. The KO efficiency was confirmed by real-time quantitative PCR and sequencing. The real-time quantitative PCR primers (5′-TCAACTGGTAGCCAGAAGACAG-3′ and 5′-TGCTGATGTAGTCTTCGGTCC-3′) span the Cas9 targeted region and the neighboring region.

Statistics and reproducibility

No statistical methods were used to predetermine sample sizes, but our sample sizes are similar to those reported in previous publications[39,40,65,72], as indicated in the figure legends. Mice were randomly allocated to experimental conditions. Each animal was given a sequential blind number on arrival. The order of treatments and stimulus presentations was randomized across animals and sessions. Data collection was not performed blind to group allocation but data analysis was performed blind to group allocation. Animals or data points excluded from specific analyses are described above and noted in figure legends. Statistical analysis was carried out using GraphPad Prism 9 (GraphPad Software) or R (v4.1.0). Gaussian distribution of the data was assessed using Shapiro–Wilk normality test, Kolmogorov–Smirnov normality test or D'Agostino and Pearson's normality test. If the data pass the Gaussian distribution test, parametric tests (paired or unpaired Student's *t*-test for two groups; one-way analysis of variance (ANOVA) for three or more groups) were used. Otherwise or for data in small sample size (<4), nonparametric tests (Wilcoxon's matched-pair signed-rank test for paired groups, the Mann–Whitney *U*-test for two unpaired groups or the Kruskal–Wallis test and Friedman's test for three or more groups) were used. Two-way ANOVA was used for experiments containing two independent variables. A mixed-effects model with Geisser–Greenhouse correction was used for one-way ANOVA or two-way ANOVA of data from matched or repeated measurements. For multiple comparisons, all other groups were compared to the control group and the two-stage step-up method of Benjamini, Krieger and Yekutieli was used for *P* value correction. The 95% confidence intervals for brain state probabilities were calculated using a bootstrap procedure: for an experimental group of n mice, with mouse i comprising m_i trials, we repeatedly resampled the data by randomly drawing for each mouse m_i trials (random sampling with replacement); for each of the 10,000 iterations, we recalculated the mean probabilities for each brain state across the n mice; the lower and upper confidence intervals were then extracted from the distribution of the resampled mean values; to test whether a given brain state is significantly modulated by laser stimulation, for each bootstrap iteration we calculated the difference between the mean probabilities during laser stimulation and the preceding period of identical duration. All statistical tests were two-tailed. All data are represented as the mean ± s.e.m. and n refers to the number of mice except for additional states. $^*P < 0.05$, $^{**}P < 0.01$, $^{***}P < 0.001$.

Reporting summary

Further information on research design is available in the Nature Portfolio Reporting Summary linked to this article.

Data availability

The scRNA-seq data are available from the National Center for Biotechnology Information's Gene Expression Omnibus (accession no. GSE218624). All other data are available in the main text or Supplementary Information.

Code availability

The customized code used for data analysis and generating figures in this study is publicly available on GitHub (https://github.com/Huatengcao/Tryptamine_sleep_homeostasis).

References

65. Zhang, Z. et al. An excitatory circuit in the perioculomotor midbrain for non-REM sleep control. *Cell* **177**, 1293–1307 (2019).
66. Barger, Z., Frye, C. G., Liu, D., Dan, Y. & Bouchard, K. E. Robust, automated sleep scoring by a compact neural network with distributional shift correction. *PLoS ONE* **14**, e0224642 (2019).
67. McIntyre, C., Saville, J. & Fuller, M. Collection of cerebrospinal fluid from murine lateral ventricles for biomarker determination in mucopolysaccharidosis type IIIA. *J. Neurosci. Methods* **324**, 108314 (2019).
68. Niemantsverdriet, E., Struyfs, H., Duits, F., Teunissen, C. E. & Engelborghs, S. in *Cerebrospinal Fluid in Clinical Neurology* (eds Deisenhammer, F. et al.) 35–57 (Springer International Publishing, 2015).
69. Wang, K. et al. Unveiling tryptophan dynamics and functions across model organisms via quantitative imaging. *BMC Biol.* **22**, 258 (2024).
70. Jiang, T. et al. MicroRNA-218 regulates neuronal radial migration and morphogenesis by targeting Satb2 in developing neocortex. *Biochem. Biophys. Res. Commun.* **647**, 9–15 (2023).
71. Jiang, T. et al. Cell-autonomous action of Slit2 in radial migration of cortical projection neurons. *Front. Mol. Neurosci.* **17**, 1505434 (2024).
72. Feng, C. et al. Cold-sensitive ventromedial hypothalamic neurons control homeostatic thermogenesis and social interaction-associated hyperthermia. *Cell Metab.* **34**, 888–901 (2022).
73. Sherathiya, V. N., Schaid, M. D., Seiler, J. L., Lopez, G. C. & Lerner, T. N. GuPPy, a Python toolbox for the analysis of fiber photometry data. *Sci. Rep.* **11**, 24212 (2021).

74. Peng, W. et al. Regulation of sleep homeostasis mediator adenosine by basal forebrain glutamatergic neurons. *Science* **369**, eabb0556 (2020).
75. Wu, Y. E., Pan, L., Zuo, Y., Li, X. & Hong, W. Detecting activated cell populations using single-cell RNA-seq. *Neuron* **96**, 313–329 (2017).
76. Duan, L. et al. PDGFRbeta cells rapidly relay inflammatory signal from the circulatory system to neurons via chemokine CCL2. *Neuron* **100**, 183–200 (2018).
77. Kim, D. W. et al. Multimodal analysis of cell types in a hypothalamic node controlling social behavior. *Cell* **179**, 713–728 (2019).
78. Shelley, J. C. et al. Epik: a software program for pK(a) prediction and protonation state generation for drug-like molecules. *J. Comput. Aided Mol. Des.* **21**, 681–691 (2007).
79. Greenwood, J. R., Calkins, D., Sullivan, A. P. & Shelley, J. C. Towards the comprehensive, rapid, and accurate prediction of the favorable tautomeric states of drug-like molecules in aqueous solution. *J. Comput. Aided Mol. Des.* **24**, 591–604 (2010).
80. Cao, H. et al. Retinoid X Receptor alpha regulates DHA-dependent spinogenesis and functional synapse formation in vivo. *Cell Rep.* **31**, 107649 (2020).
81. Zuo, E. et al. One-step generation of complete gene knockout mice and monkeys by CRISPR/Cas9-mediated gene editing with multiple sgRNAs. *Cell Res.* **27**, 933–945 (2017).
82. Concordet, J. P. & Haeussler, M. CRISPOR: intuitive guide selection for CRISPR/Cas9 genome editing experiments and screens. *Nucleic Acids Res.* **46**, W242–W245 (2018).

Acknowledgements

We thank M.-M. Poo, Y. Dan, W. Wisden and X. Yu for commenting on the paper. We thank K. Zhang for help establishing the SD system. We thank R. Tao for discussing the development of the TrpA sensor. We thank N. Gao, X. Hu, C. Feng and H. Zhou for help in constructing and packaging CRISPR–Cas9 AAVs. We thank X. Jiang, X. Xu, X. Yang, Q. Liu and all the members of Z. Zhang's laboratory for technical support and helpful discussions.

Author contributions

H.C., P.Y. and Z.Z. conceived of this research. H.C. performed all experiments and data analyses unless otherwise stated, with the help of J.Z., Y.X., S.H., S.P. and Q.Z. K.W., Q.Z., J.C., H.W. and Y.M. developed the TrpA sensor. Z.-H.Z., X.L., Z.-J.L. and T.H. analyzed molecular structures and conducted intracellular calcium mobilization assay. X.N.Z., K.X.Y. and J.H. conducted the electrophysiology experiments. B.W. and J.-t.Y. performed genome-wide association studies. Z.Z. supervised the project. H.C., Z.H., P.Y. and Z.Z. wrote the paper. All authors read and approved the paper.

Funding

This work was supported by National Key Research and Development Program of China (2024YFA1802702 to Z.Z., 2023YFC2506201 to H.C. and 2023YFC3603200 to P.Y.), the National Science and Technology Innovation 2030 grants (2022ZD0206100 to Z.Z.), the National Natural Science Foundation of China grants (U23A20433 to Z.Z., 32371036 to P.Y. and 32100799 to H.C.), Lingang Laboratory grants (LGL-6672-21 to Z.Z. and LGL-6672-19 to P.Y.), the China Postdoctoral Science Foundation (2020TQ0332 and 2020M681415 to H.C.) and Space Medical Experiment Project of CMSP (HYZHXMN0100 to Z.Z.). P.Y. was further supported by the Shanghai Pilot Program for Basic Research, FuDan University 21TQ1400100 (22TQ019) and Scientific Research Innovation Capability Support Project for Young Faculty (SRICSPYF-ZY2025105).

Competing interests

The authors declare no competing interests.

Additional information

Extended data is available for this paper at https://doi.org/10.1038/s41593-026-02332-x.

Supplementary information The online version contains supplementary material available at https://doi.org/10.1038/s41593-026-02332-x.

Correspondence and requests for materials should be addressed to Yu Mu, Zhian Hu, Peng Yuan or Zhe Zhang.

Peer review information *Nature Neuroscience* thanks Luis de Lecea, Michael Lazarus and the other, anonymous, reviewer(s) for their contribution to the peer review of this work.

https://doi.org/10.1038/s41593-026-02332-x

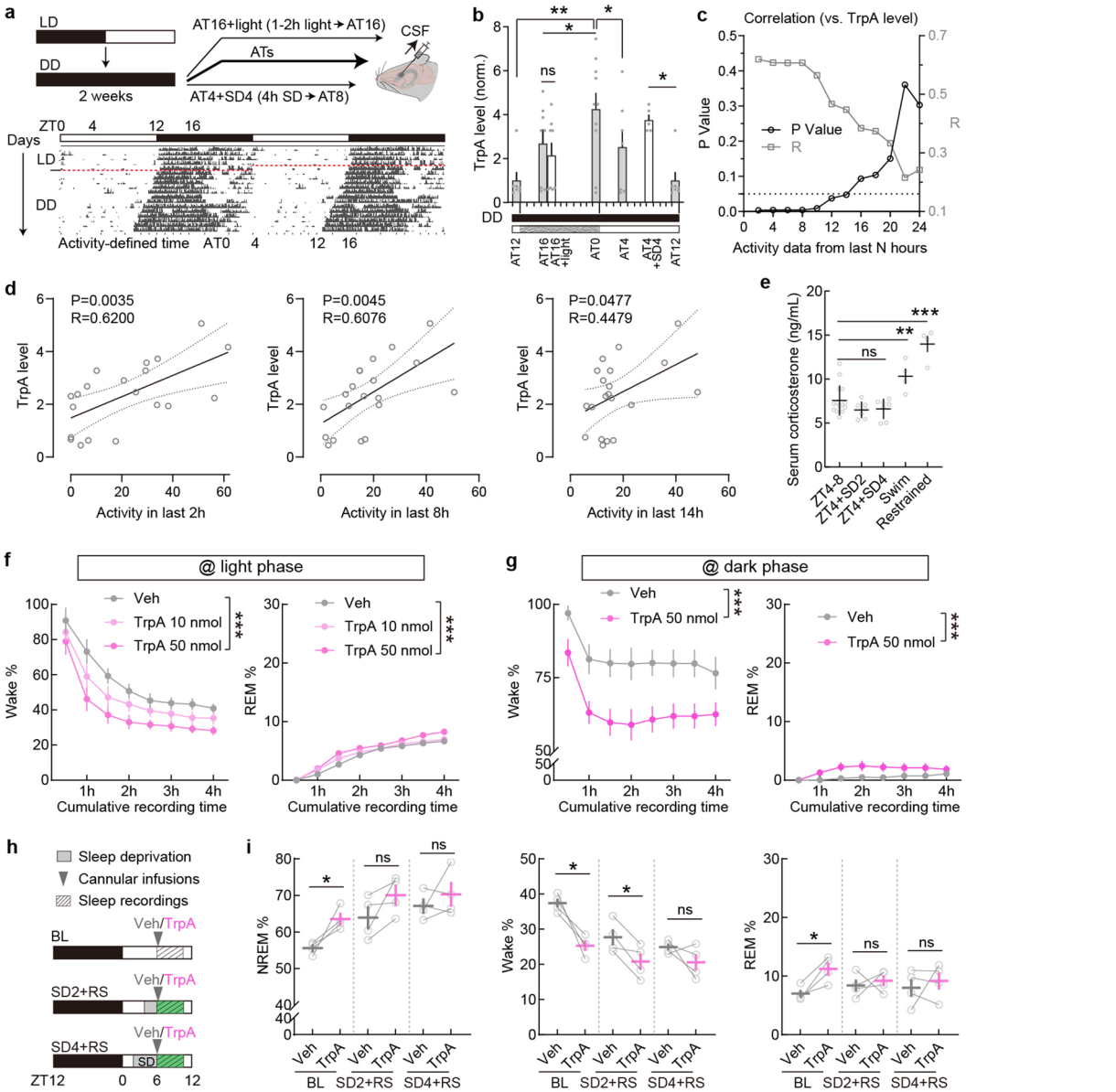

Extended Data Fig. 1 | Tryptamine reflects sleep pressure and improves homeostatic sleep. a,b, Schematic (**a**) and summary data (**b**) of the measurements of TrpA dynamics from intrinsic period-shifted mice in all dark condition. AT12/AT4: N = 7 mice, AT16/AT16+light: N = 8, AT0: N = 10, AT4 + SD4: N = 5, one-way ANOVA followed by multiple comparisons. P values: AT0 vs. AT12, 0.0012; AT0 vs. AT16, 0.0468; AT0 vs. AT4, 0.0468; AT16 vs. AT16+light, 0.3349; AT4 + SD4 vs. ZT12, 0.0136. **c,d**, Correlation analysis of recent animal activity (**c**) and CSF TrpA level (**d**). Data from (a,b) with locomotion activity collected by running-wheels. "P value" and "R" were calculated by Pearson correlation test. **e**, Serum corticosterone levels in BL and SD mice, and in stressed mice with forced swim or acutely restrained. N = 15 mice in ZT4-8 group, N = 7 mice in ZT4 + SD2 group and in ZT4+SD4 group, N = 4 mice in swim group and in restrained group, one-way ANOVA followed by multiple comparisons. P values: ZT4-8 vs. ZT4+SD2, 0.0902; ZT4-8 vs. ZT4+SD4, 0.0909; ZT4-8 vs. Swim, 0.0031; ZT4-8 vs. Restrained, <0.0001. **f**, Cumulative percentages of brain states after vehicle and TrpA administrations. 8 paired infusions and recordings from 4 mice per group, two-way ANOVA followed by multiple comparisons (compare group means). P values: <0.0001 (in left) and 0.0007 (in right). **g**, Same as (**f**) but for TrpA treatments and recordings in dark phase. Two-way ANOVA, P values in left and right: <0.0001. **h,i**, Schematic (**h**) and quantitative data (**i**) of TrpA infusion experiments in BL and SD conditions. N = 4 mice per group, paired t-test. P values in NREM%: BL, 0.0390; SD2+RS, 0.1283; SD4+RS, 0.4353. P values in Wake%: BL, 0.0178; SD2+RS, 0.0379; SD4+RS, 0.2344. P values in REM%: BL, 0.0255; SD2+RS, 0.6928; SD4+RS, 0.6295. Data are presented as mean ± SEM; all statistical tests were two-sided; P values are as indicated in graphs: ns, not significant (P > 0.1), *P < 0.05, **P < 0.01, ***P < 0.001.

https://doi.org/10.1038/s41593-026-02332-x

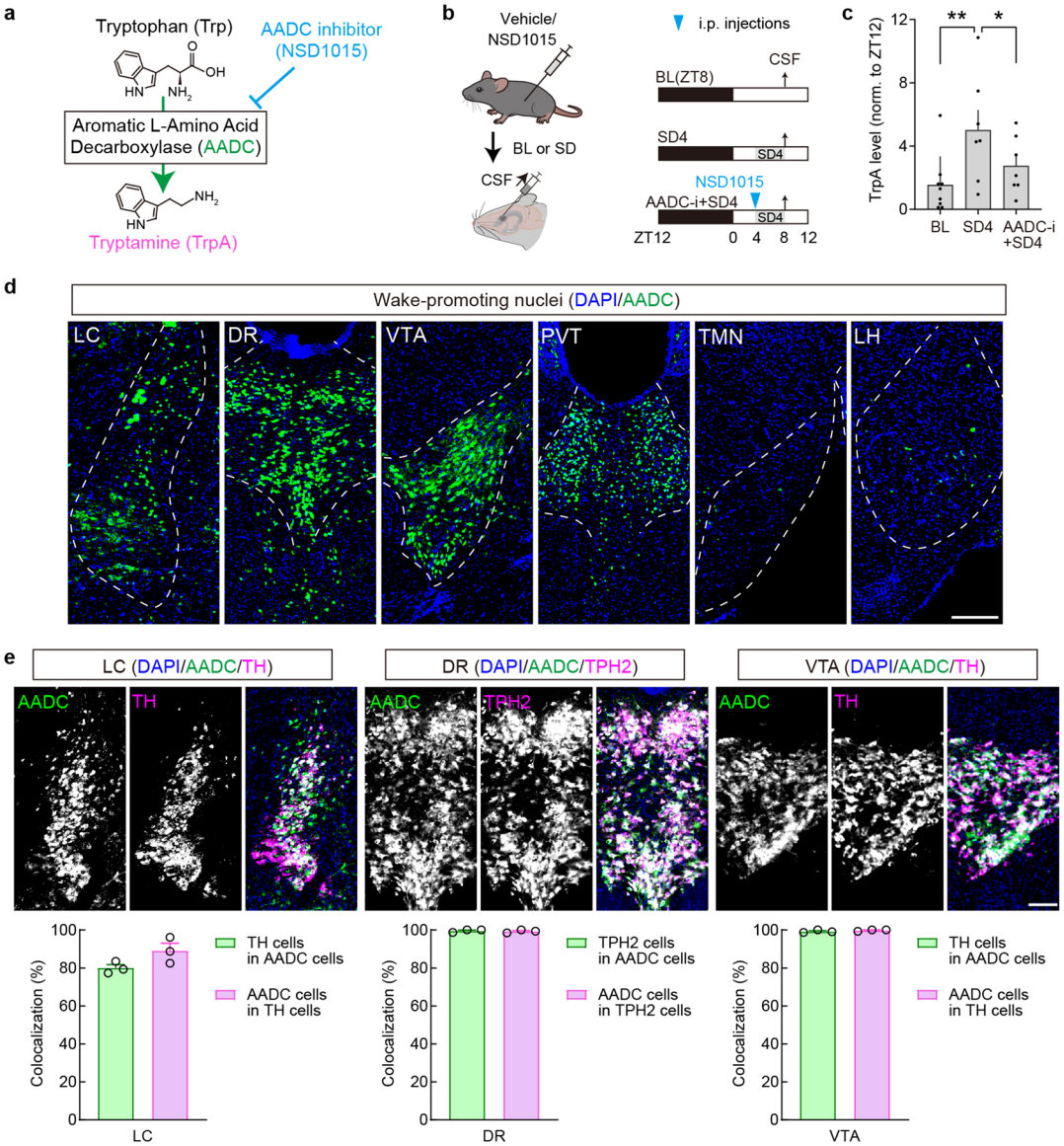

Extended Data Fig. 2 | AADC is highly expressed in monoaminergic neurons. **a**, Diagram of enzymatic action of AADC in catalyzing Trp decarboxylation to produce TrpA. **b**, Schematics of AADC inhibitor injections, SD, and CSF collections. **c**, Normalized (to ZT12) TrpA level in (**b**). BL: N = 9 mice, SD4/ AADC_i+SD4: N = 7 mice, one-way ANOVA followed by multiple comparisons. P values: SD4 vs. BL, 0.0097; SD4 vs. AADC-i+SD4, 0.0485. **d**, Representative images of AADC expression in some wake-promoting nuclei. These experiments were independently repeated ≥ 3 times with similar results. Scale bar, 100 µm. LC, locus coeruleus; DR, dorsal raphe; VTA, ventral tegmental area; PVT, paraventricular nucleus of the thalamus; TMN, tuberomammillary nucleus; SC, superior colliculus; **e**, Representative images and quantifications showing that AADC is expressed in the monoaminergic neurons in the LC (TH for norepinephrine neurons), DR (TPH2 for serotonin neurons) and VTA (TH for dopamine neurons). 3 mice per group. Scale bar, 100 µm. Data are presented as mean ± SEM; all statistical tests were two-sided; P values are as indicated in graphs: *P < 0.05, **P < 0.01.

https://doi.org/10.1038/s41593-026-02332-x

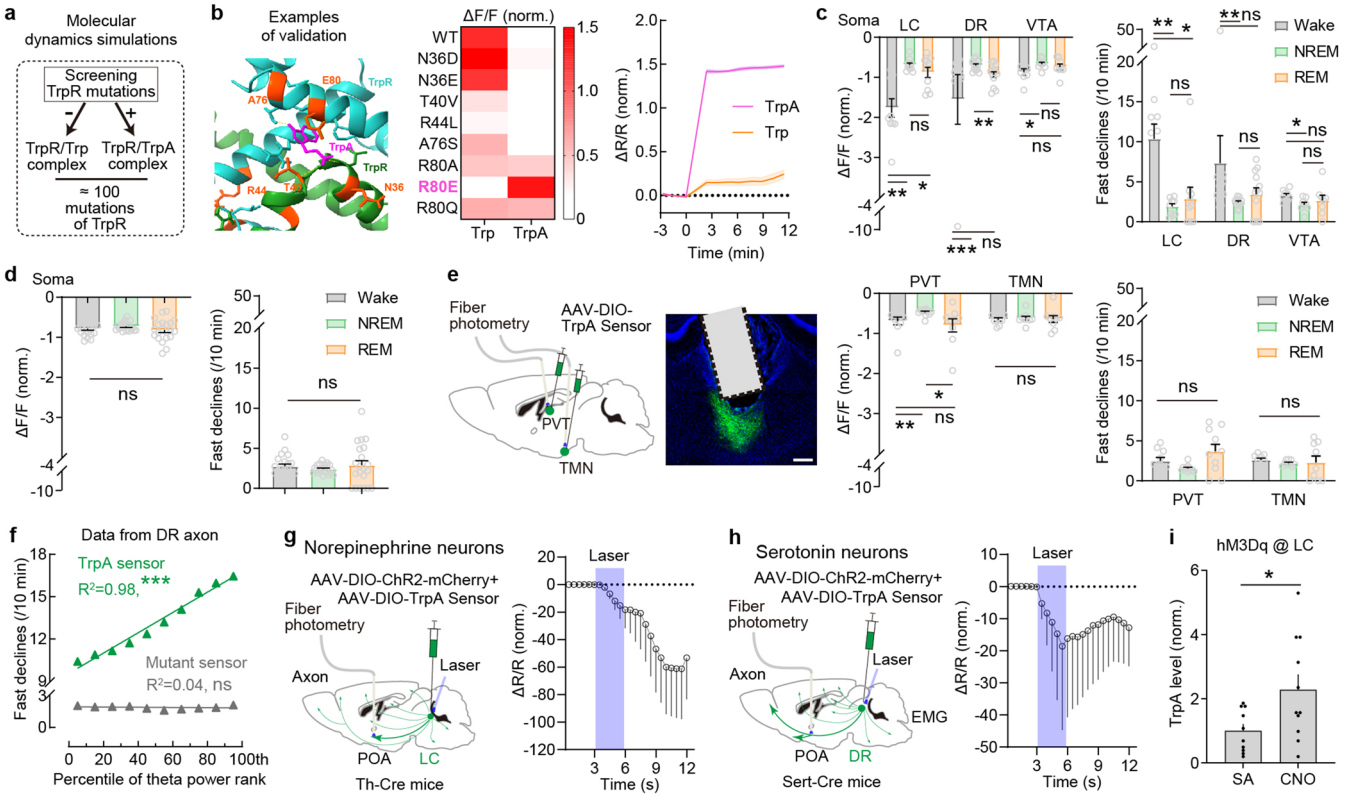

Extended Data Fig. 3 | Generation of an effective TrpA sensor, and dynamic TrpA levels in monoaminergic system. a, Molecular dynamics simulations screened out about 100 point-mutations in TrpR that likely enhancing its reaction to TrpA, and reducing the reaction to Trp. **b**, Validation data of 8 examples of our tested mutants. The crystal structure showed the amino acid residues closed to the binding site of TrpA in TrpR (left); the responses of constructed sensors, based on the predicted mutants, after Trp (100 μM) or TrpA (100 μM) administration in E. coli cells (right). Among which, the mutant R80E based sensor (TrpA sensor) selectively responded to TrpA, but not Trp. **c**, Quantitative data of TrpA sensor signal in the somas of monoaminergic neurons (LC^{Th}, DR^{Sert} and VTA^{DAT} neurons), shown as the averaged ΔF/F and the fast declines of the signal, to demonstrate TrpA release. LC: N = 10 sessions, DR: N = 13 sessions, VTA: N = 8 sessions, ≥ 3 mice per group, Wilcoxon matched-pairs signed rank test. P values in left: LC (Wake vs. NREM, 0.0020; Wake vs. REM, 0.0371; NREM vs. REM, 0.1309); DR (Wake vs. NREM, 0.0005; Wake vs. REM, 0.8394; NREM vs. REM, 0.0061); VTA (Wake vs. NREM, 0.0156; Wake vs. REM, 0.1094; NREM vs. REM, 0.7422). P values in right: LC (Wake vs. NREM, 0.0039; Wake vs. REM, 0.0371; NREM vs. REM, >0.9999); DR (Wake vs. NREM, 0.0046; Wake vs. REM, 0.3757; NREM vs. REM, 0.1909); VTA (Wake vs. NREM, 0.0156; Wake vs. REM, 0.3125; NREM vs. REM, 0.9453). **d**, Same as (c) but for control Mutant sensor. 21 recordings (LC*12+DR*5+VTA*4) from 6 mice, Wilcoxon matched-pairs signed rank test. **e**, Same as (c) but for TrpA signal in the somas of glutaminergic neurons in the PVT and histaminergic neurons (TMN^{Gad2} neurons). PVT: N = 10 sessions, TMN: N = 9 sessions, 3 mice per group, Wilcoxon matched-pairs signed rank test. P values in middle: PVT (Wake vs. NREM, 0.0098; Wake vs. REM, 0.6250; NREM vs. REM, 0.0273); TMN (Wake vs. NREM, 0.3594; Wake vs. REM, 0.9102; NREM vs. REM, >0.9999). P values in right: PVT (Wake vs. NREM, 0.1055; Wake vs. REM, 0.5566; NREM vs. REM, 0.2324); TMN (Wake vs. NREM, 0.1641; Wake vs. REM, 0.8203; NREM vs. REM, 0.7344). Scale bar, 100 μm. **f**, Correlation between the TrpA/Mutant sensor activity with EEG theta power (data from DR axon). Simple linear regression, P values: TrpA Sensor, <0.0001; Mutant sensor, 0.5767. **g**, Schematic and summary data of TrpA sensor recordings in the axons of LC^{NE} neurons with optogenetic activation. N = 280 trials from 6 recording sessions from 2 mice. **h**, Same as (f) but for the axons of $DR^{5\text{-}HT}$ neurons. N = 561 trials from 16 recording sessions from 3 mice. **i**, Normalized TrpA level in CSF from mice with LC^{NE} neuronal activation by chemogenetics (CNO). Samples were collected in 3-4 h after Veh (Saline)/CNO injections, Veh: N = 10 mice, CNO: N = 11 mice, two-tailed unpaired t-test, P = 0.0294. Data are presented as mean ± SEM; all statistical tests were two-sided; P values are as indicated in graphs: ns, not significant (P > 0.1), *P < 0.05, **P < 0.01, ***P < 0.001.

https://doi.org/10.1038/s41593-026-02332-x

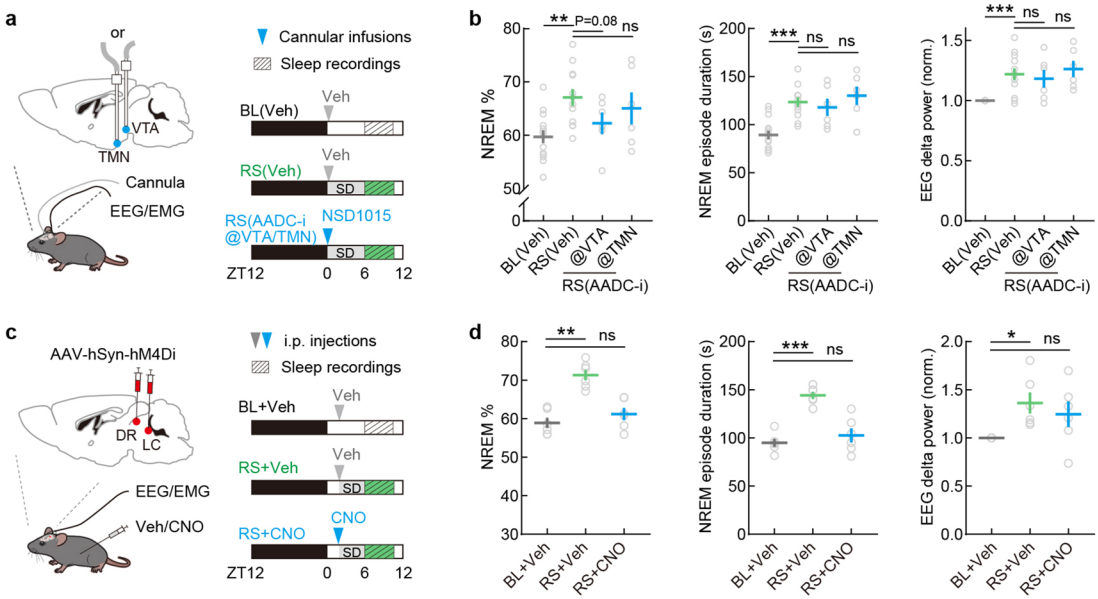

Extended Data Fig. 4 | Tryptamine production or neuronal activity in the LC and DR is required for homeostatic sleep rebound. a,b, Schematics (**a**) and summary data (**b**) for the experiment of sleep rebound recordings with Veh/AADC-inhibitor cannular infusions in VTA or TMN. BL and RS groups: N = 12 recordings from 6 mice, RS(AADC_i) groups: N = 6 recordings from 3 mice, one-way ANOVA followed by multiple comparisons. P values in left: RS(Veh) vs. BL(Veh), 0.0027; RS(Veh) vs. RS(AADC-i)@VTA, 0.0824; RS(Veh) vs. RS(AADC-i)@TMN, 0.3130. P values in middle: RS(Veh) vs. BL(Veh), < 0.0001; RS(Veh) vs. RS(AADC-i)@VTA, 0.3938; RS(Veh) vs. RS(AADC-i)@TMN, 0.3938. P values in right: RS(Veh) vs. BL(Veh), 0.0005; RS(Veh) vs. RS(AADC-i)@VTA, 0.4066; RS(Veh) vs. RS(AADC-i)@TMN, 0.4066. **c,d**, Schematics (**c**) and summary data (**d**) for the experiment of sleep rebound recordings with chemogenetic inhibition (CNO) in LC and DR. N = 6 recording sessions from 3 mice, one-way ANOVA followed by multiple comparisons. P values in left: BL+Veh vs. RS+Veh, 0.0028; BL+Veh vs. RS+CNO, 0.6275. P values in middle: BL+Veh vs. RS+Veh, 0.0001; BL+Veh vs. RS+CNO, 0.4833. P values in right: BL+Veh vs. RS+Veh, 0.0355; BL+Veh vs. RS+CNO, 0.2037. Data are presented as mean ± SEM; all statistical tests were two-sided; P values are as indicated in graphs: ns, not significant (P > 0.1), *P < 0.05, **P < 0.01, ***P < 0.001.

https://doi.org/10.1038/s41593-026-02332-x

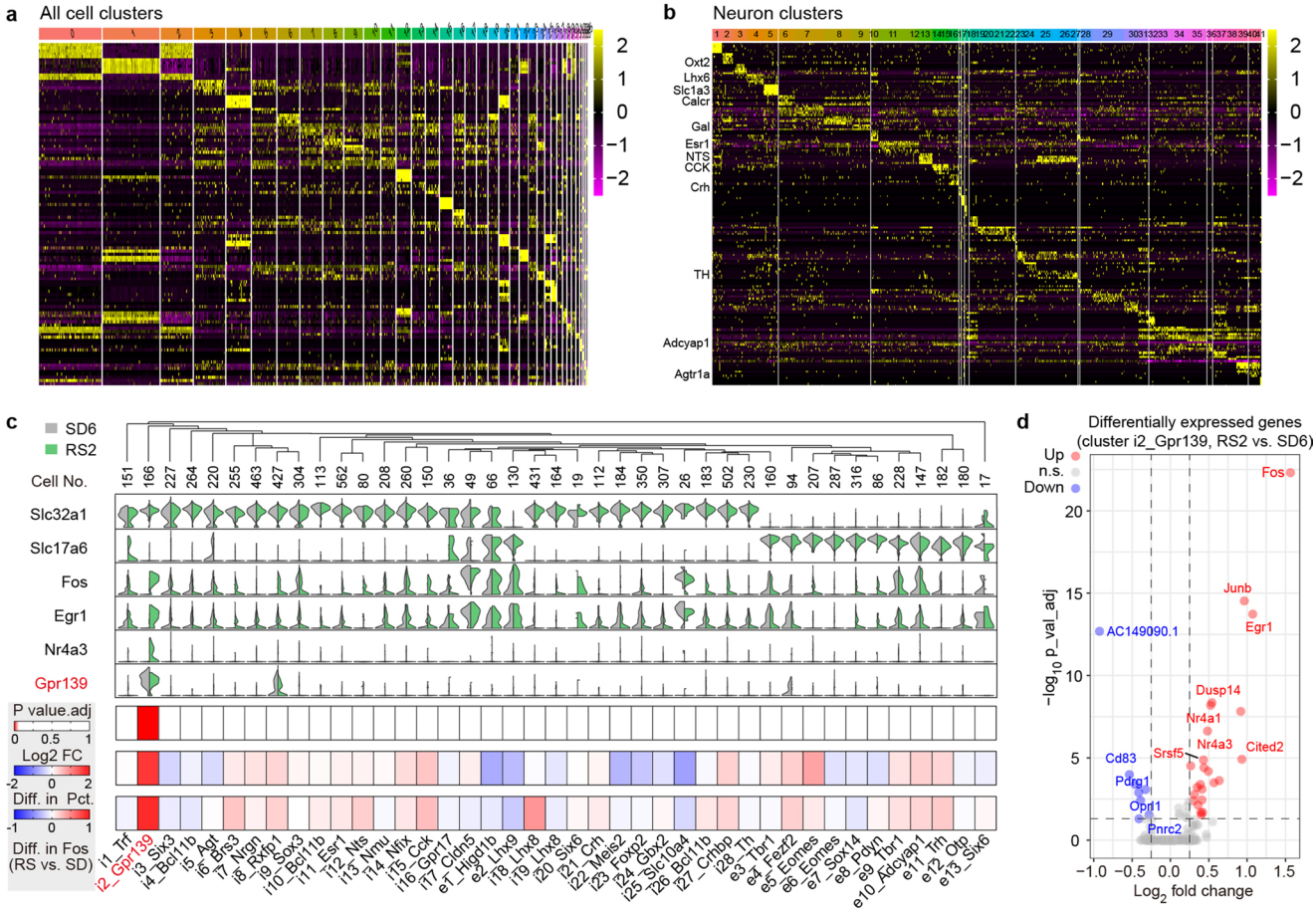

Extended Data Fig. 5 | scRNA-Seq identifies an intrinsic transcriptomic neuronal cluster expressing *Gpr139* in the POA selectively responded to homeostatic sleep. a, Heatmap plot of top 5 markers in each cell cluster present distinct expression patterns upon unsupervised clustering analysis. **b**, Top 5 markers of each neuronal cluster present distinct expression patterns, labeled with several previously reported sleep relevant genes. **c**, Violin plot of log-normalized expression of immediate early genes and cell-type-defining genes in each neuronal clusters, with the phylogenetic tree and the cell numbers; and heatmaps of the adjusted P value, the log fold-change and the difference in detected cell percentage of Fos expression between RS2 and SD6 groups in these clusters. Wilcoxon Rank Sum test followed by bonferroni correction. **d**, Volcano plot of differentially expressed genes in i2_Gpr139 neurons between RS2 and SD6 groups. Wilcoxon Rank Sum test followed by bonferroni correction.

https://doi.org/10.1038/s41593-026-02332-x

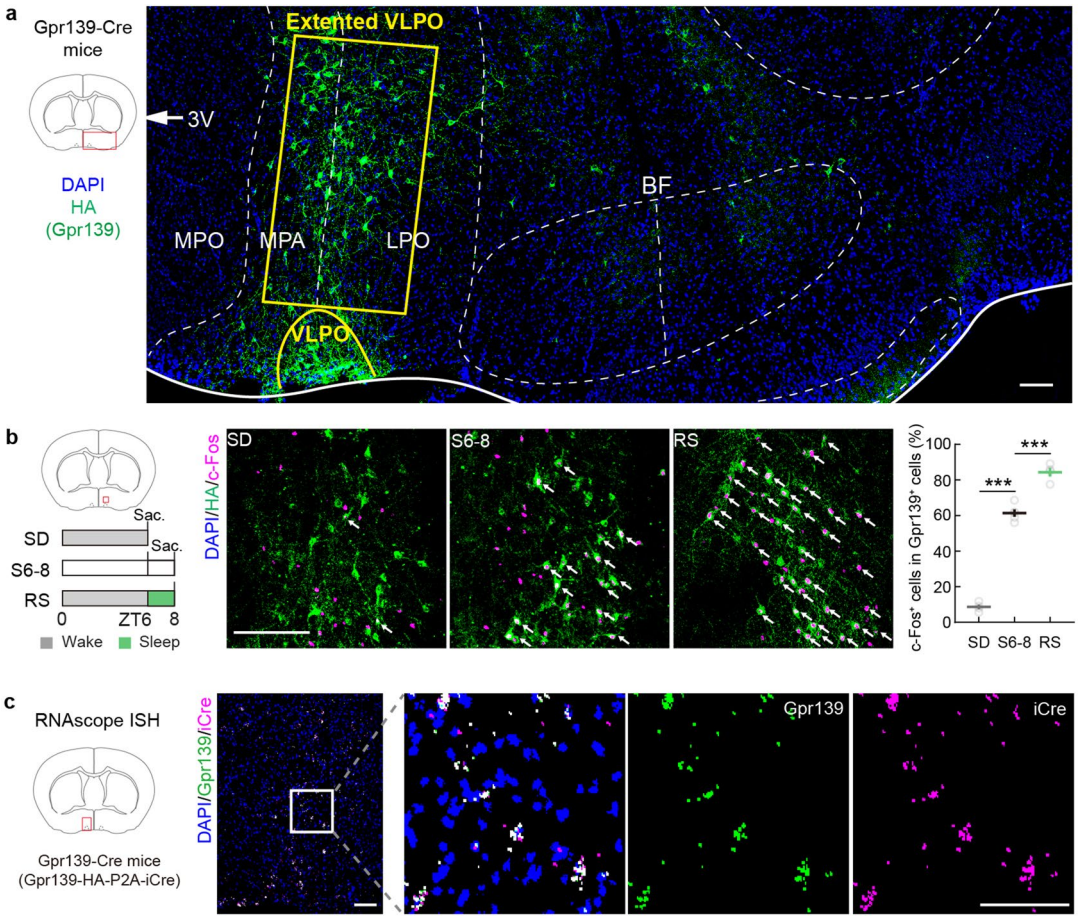

Extended Data Fig. 6 | Verification of the location and sleep state-related activation of *Gpr139* neurons in the POA. a, HA immunostaining indicating the location of Gpr139 neurons in the POA. The red box in the left indicates the location of the image. The experiment was independently repeated ≥ 3 times with similar results. Scale bar, 100 µm. **b**, Representative images and quantitative result of c-Fos immunostaining in SD (wakefulness, N = 4 mice), S6-8 (*ad libitum* sleep, N = 5 mice) and RS (2 h RS after SD, N = 4 mice) conditions, suggesting that POA^{Gpr139} neurons activated during sleep and more activated after SD (rebound sleep). The red box indicates the location of the images. Scale bar, 100 µm. One-way ANOVA followed by multiple comparisons. All P values < 0.0001. **c**, In Gpr139-Cre mice, *Gpr139* and iCre showed extremely high colocalization. The experiment was independently repeated ≥ 3 times with similar results. Scale bar, 100µm. Data are presented as mean ± SEM; all statistical tests were two-sided; P values are as indicated in graphs: ***P < 0.001.

https://doi.org/10.1038/s41593-026-02332-x

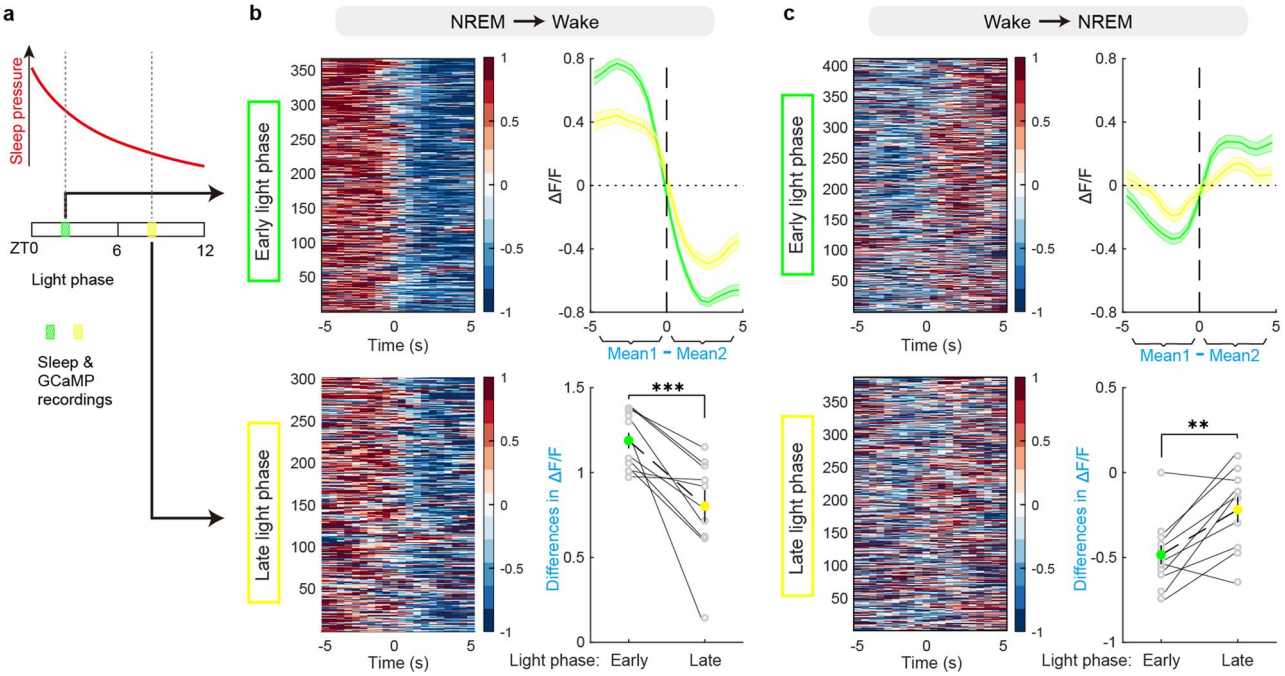

Extended Data Fig. 7 | Activity change of POA^{Gpr139} neurons during sleep-wake transition is more pronounced in high sleep pressure periods. a-c, Schematic (**a**) and the z-scored calcium activity of POA^{Gpr139} neurons around NREM to wake transitions (**b**) and wake to NREM transitions (**c**). Heatmaps (left) show the calcium activity of individual transitions from early light phase (**b**) or late light phase (**c**). Upper right panels show the average calcium activity around transitions. Bottom right panels show average differences of calcium activity between Mean1 (before transition) and Mean2 (after transition) in recording sessions from early light phase (**b**) or late light phase (**c**). Early light phase: N = 12 recording sessions from 4 mice, late light phase: N = 10 recording sessions from 4 mice, unpaired t-test. P values: 0.0009 (b) and 0.0091 (c). Data are presented as mean ± SEM; all statistical tests were two-sided; P values are as indicated in graphs: **P < 0.01.

https://doi.org/10.1038/s41593-026-02332-x

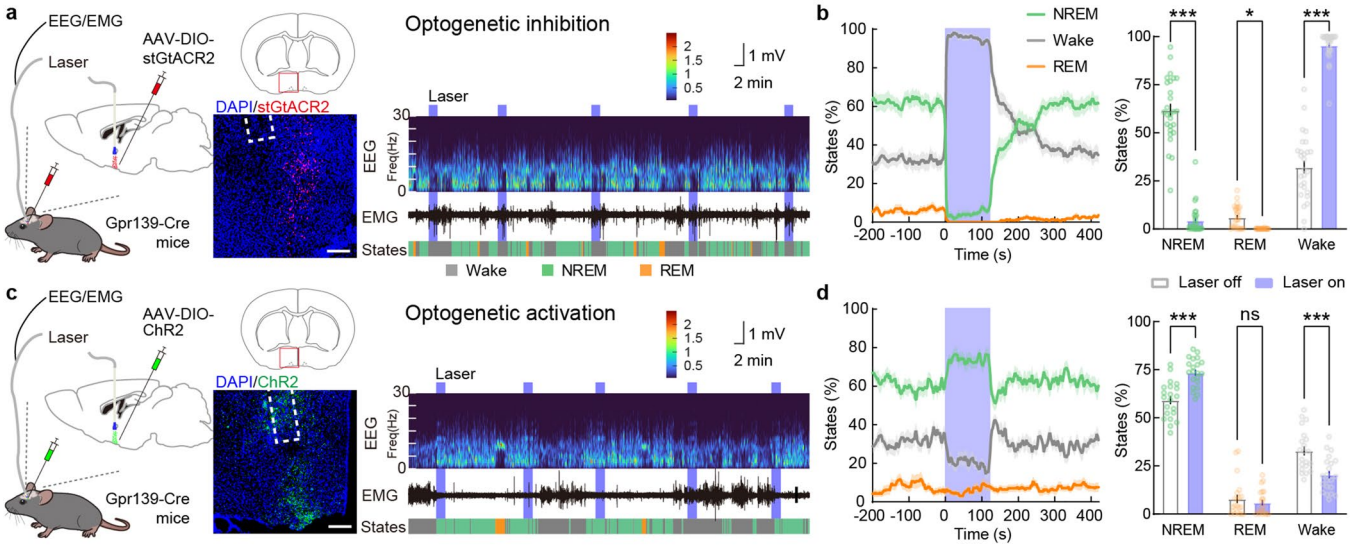

Extended Data Fig. 8 | The activity of POA^{Gpr139} neurons bidirectionally regulate sleep. a, Schematics and representative image and examples of brain states, EEG spectrogram and EMG trace for optogenetic inhibition experiments in Gpr139-Cre mice with AAV-DIO-GtACR2 injected. Scale bar, 200 μm. **b**, Summary data of brain state percentages in (**a**). A line graph (left) presenting a 620 s duration around laser on (200 s before laser on, 120 s during laser on and 300 s after laser on); and a bar graph (right) presenting state quantifications before (laser off, 120 s) and during laser on (120 s). N = 27 sessions from 9 mice, 3 sessions per mouse. Laser stimulation significantly decreased NREM sleep (left: $P < 0.0001$, bootstrap; right: $P < 0.0001$, two-way ANOVA followed by multiple comparisons) and REM sleep (left: $P < 0.0001$, bootstrap; right: $P = 0.0487$, two-way ANOVA followed by multiple comparisons), and increased wakefulness (left: $P < 0.0001$, bootstrap; right: $P < 0.0001$, two-way ANOVA followed by multiple comparisons). **c,d**, Same as (**a** and **b**) but for optogenetic activation experiments in Gpr139-Cre mice with AAV-DIO-ChR2 injected. N = 21 sessions from 5 mice. Laser stimulation significantly increased NREM sleep (left: $P < 0.0001$, bootstrap; right: $P < 0.0001$, two-way ANOVA followed by multiple comparisons) and decreased wakefulness (left: $P < 0.0001$, bootstrap; right: $P < 0.0001$, two-way ANOVA followed by multiple comparisons). Data are presented as mean ± SEM; all statistical tests were two-sided; P values are as indicated in graphs: ns, not significant ($P > 0.1$), *$P < 0.05$, ***$P < 0.001$.

https://doi.org/10.1038/s41593-026-02332-x

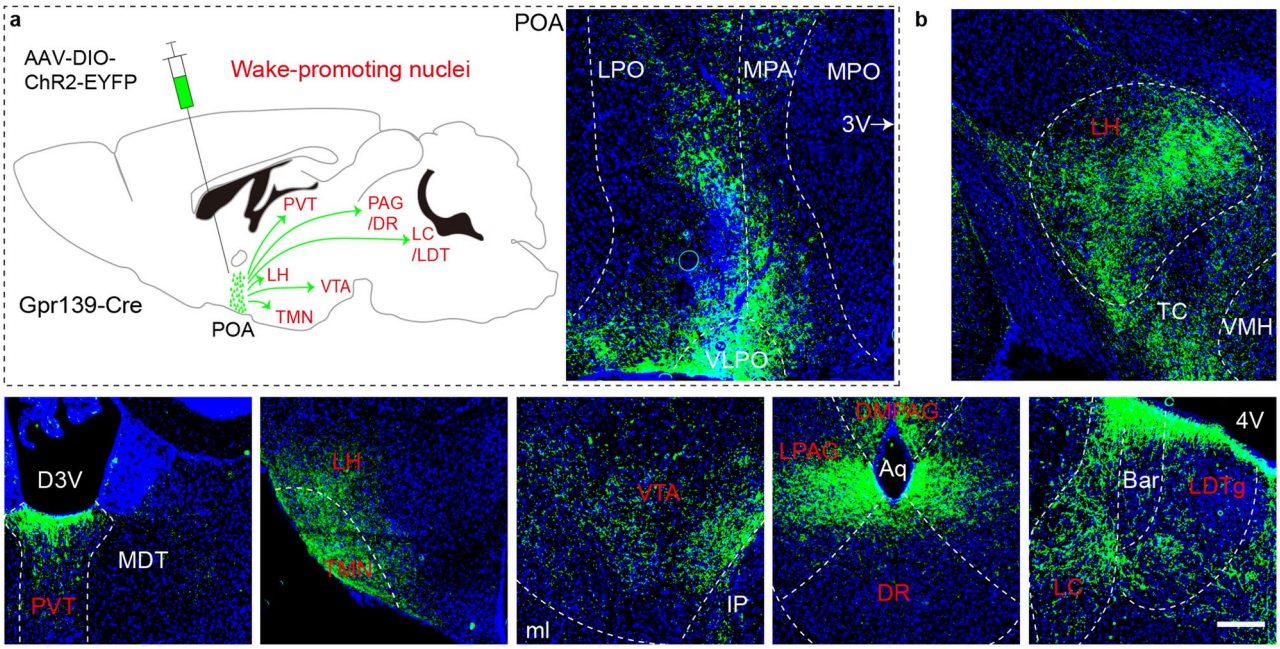

Extended Data Fig. 9 | POA^{Gpr139} neurons project onto multiple wake-promoting nuclei. a,b, Schematic and example images of the viral injection site (**a**) and the projection map of POA^{Gpr139} neurons onto wake-promoting nuclei (**b**). LPO, lateral preoptic area; MPA, medial preoptic area; 3 V, 3rd ventricle; LH, lateral hypothalamus; TC, tuber cinereum area; VMH, ventromedial hypothalamic nucleus; D3V, dorsal 3rd ventricle; PVT, paraventricular thalamic nucleus; MDT, mediodorsal thalamic nucleus; TMN, tuberomammillary; VTA, ventral tegmental area; ml, medial lemniscus; IP, interpeduncular nucleus; LPAG, lateral periaqueductal gray; DMPAG, dorsomedial periaqueductal gray; Aq, aqueduct; DR, dorsal raphe nucleus; LC, locus coeruleus; Bar, Barrington's nucleus; LDTg, laterodorsal tegmental nucleus; 4 V, 4th ventricle; scale bar, 200 µm.

https://doi.org/10.1038/s41593-026-02332-x

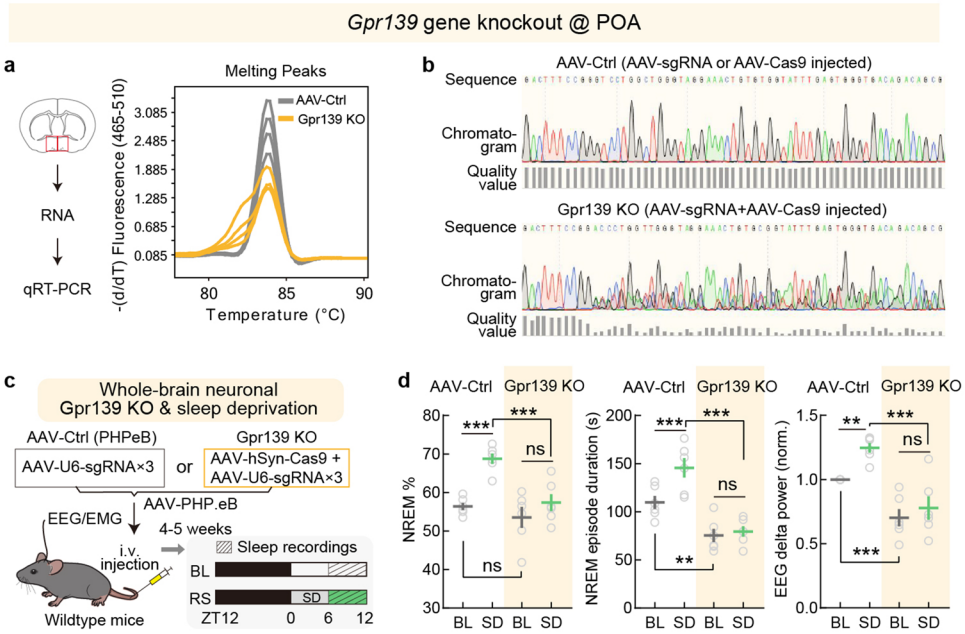

Extended Data Fig. 10 | Whole-brain *Gpr139* knockout has the same effects on baseline and recovery sleep as POA *Gpr139* knockout. a, qRT-PCR melting curves of the tissue RNA (POA) from AAV-Ctrl and *Gpr139* knockout mice, showed partially damaged *Gpr139* mRNA (Neurons) in *Gpr139* knockout mice, compared with AAV-Ctrl mice. **b**, Sequencing results of the cDNA from the tissue RNA (POA) of AAV-Ctrl and *Gpr139* knockout mice, demonstrated the break in the targeted exon2 region of *Gpr139*. **c**, Schematic of sleep recordings in baseline (BL) and after sleep deprivation (recovery sleep, RS) conditions of AAV-PHPeB-ctrl or whole-brain *Gpr139* knockout mice. **d**, Quantification of sleep duration and depth indicated by total NREM sleep, NREM episode duration and EEG delta power in (**c**). N = 6 recording sessions from 3 mice per group, one-way ANOVA followed by multiple comparisons. P values in left: BL vs. RS, 0.0003 (Ctrl) and 0.1363 (KO); BL vs. BL, 0.1931; RS vs. RS, 0.0005. P values in middle: BL vs. RS, 0.0010 (Ctrl) and 0.1228 (KO); BL vs. BL, 0.0011; RS vs. RS, <0.0001. P values in right: BL vs. RS, 0.0022 (Ctrl) and 0.0668 (KO); BL vs. BL, 0.0008; RS vs. RS, <0.0001. Data are presented as mean ± SEM; all statistical tests were two-sided; P values are as indicated in graphs: ns, not significant (P > 0.1), **P < 0.01, ***P < 0.001.

nature portfolio

Corresponding author(s): Yu Mu, Zhian Hu, Peng Yuan, Zhe Zhang

Last updated by author(s): Apr 23, 2026

Reporting Summary

Nature Portfolio wishes to improve the reproducibility of the work that we publish. This form provides structure for consistency and transparency in reporting. For further information on Nature Portfolio policies, see our Editorial Policies and the Editorial Policy Checklist.

Statistics

For all statistical analyses, confirm that the following items are present in the figure legend, table legend, main text, or Methods section.

n/a	Confirmed	
☐	☒	The exact sample size (*n*) for each experimental group/condition, given as a discrete number and unit of measurement
☐	☒	A statement on whether measurements were taken from distinct samples or whether the same sample was measured repeatedly
☐	☒	The statistical test(s) used AND whether they are one- or two-sided *Only common tests should be described solely by name; describe more complex techniques in the Methods section.*
☐	☒	A description of all covariates tested
☐	☒	A description of any assumptions or corrections, such as tests of normality and adjustment for multiple comparisons
☐	☒	A full description of the statistical parameters including central tendency (e.g. means) or other basic estimates (e.g. regression coefficient) AND variation (e.g. standard deviation) or associated estimates of uncertainty (e.g. confidence intervals)
☐	☒	For null hypothesis testing, the test statistic (e.g. *F*, *t*, *r*) with confidence intervals, effect sizes, degrees of freedom and *P* value noted *Give P values as exact values whenever suitable.*
☒	☐	For Bayesian analysis, information on the choice of priors and Markov chain Monte Carlo settings
☒	☐	For hierarchical and complex designs, identification of the appropriate level for tests and full reporting of outcomes
☐	☒	Estimates of effect sizes (e.g. Cohen's *d*, Pearson's *r*), indicating how they were calculated

Our web collection on statistics for biologists contains articles on many of the points above.

Software and code

Policy information about availability of computer code

Data collection	TDT recording system (Synapse software) was used for polysomnographic (EEG/EMG) and fiber photometry data recordings. VS-ASW was utilized to capture immunofluorescent images. UHPLC was performed using a combined method, that the Waters UHPLC Amino Acid Analysis Solution combines UHPLC separation technology with AccQ•Tag™ Ultra Derivatization Chemistry (ACQUITY UPLC H-Class PLUS System, Waters). Multiclamp 700B were used for patch clamp data collection. scRNA-sequencing data were processed with the Cell Ranger (10X Genomics). Molecular docking was performed using Schrödinger Suite 2022-3. The binding kinetics assay using stopped-flow technique was performed with an SX20 Stopped-Flow accessory (Applied Photophysics Ltd).
Data analysis	EEG/EMG data, fiber photometry data and patch clamp data were analyzed using MATLAB (R2018b). Imaging data analysis was performed using Image J. Sequencing data were analyzed with R (V 4.1.0). Statistical analysis was carried out using GraphPad Prism 9 (GraphPad Software, La Jolla, CA, USA) or R (V 4.1.0).

For manuscripts utilizing custom algorithms or software that are central to the research but not yet described in published literature, software must be made available to editors and reviewers. We strongly encourage code deposition in a community repository (e.g. GitHub). See the Nature Portfolio guidelines for submitting code & software for further information.

Data

Policy information about availability of data

All manuscripts must include a data availability statement. This statement should provide the following information, where applicable:

- Accession codes, unique identifiers, or web links for publicly available datasets
- A description of any restrictions on data availability
- For clinical datasets or third party data, please ensure that the statement adheres to our policy

All data needed to evaluate the conclusions in the paper are present in the paper and/or the Supplementary Materials and can be obtained from the corresponding author upon reasonable request.

Research involving human participants, their data, or biological material

Policy information about studies with human participants or human data. See also policy information about sex, gender (identity/presentation), and sexual orientation and race, ethnicity and racism.

Reporting on sex and gender	N/A
Reporting on race, ethnicity, or other socially relevant groupings	N/A
Population characteristics	N/A
Recruitment	N/A
Ethics oversight	N/A

Note that full information on the approval of the study protocol must also be provided in the manuscript.

Field-specific reporting

Please select the one below that is the best fit for your research. If you are not sure, read the appropriate sections before making your selection.

☒ Life sciences ☐ Behavioural & social sciences ☐ Ecological, evolutionary & environmental sciences

For a reference copy of the document with all sections, see nature.com/documents/nr-reporting-summary-flat.pdf

Life sciences study design

All studies must disclose on these points even when the disclosure is negative.

Sample size	Sample sizes were chosen to reliably measure experimental effects while minimizing the number of animals used in accordance with ethical guidelines. Sample size was determined based on similar previously published studies in the same field.
Data exclusions	All collected data were included in the study.
Replication	We confirmed our main findings by repeating recordings and behavioral experiments in multiple animals, and repeating all recordings in the same animal whenever possible. All attempts at replication were successful.
Randomization	Animals were randomly assigned to control or different experimental groups.
Blinding	Each animal was given a sequential blind number upon arrival. The order of treatments and stimulus presentations was randomized across animals and sessions. Data collection was not performed blind to group allocation. Data analysis was performed blind to group allocation.

Reporting for specific materials, systems and methods

We require information from authors about some types of materials, experimental systems and methods used in many studies. Here, indicate whether each material, system or method listed is relevant to your study. If you are not sure if a list item applies to your research, read the appropriate section before selecting a response.

Materials & experimental systems

n/a	Involved in the study
☐	☒ Antibodies
☐	☒ Eukaryotic cell lines
☒	☐ Palaeontology and archaeology
☐	☒ Animals and other organisms
☒	☐ Clinical data
☒	☐ Dual use research of concern
☒	☐ Plants

Methods

n/a	Involved in the study
☒	☐ ChIP-seq
☒	☐ Flow cytometry
☒	☐ MRI-based neuroimaging

Antibodies

Antibodies used

rabbit anti-DOPA Decarboxylase (anti-AADC, Abcam, Cat# ab3905, RRID: AB_304145), rabbit anti-Fos (SynapticSystem, Cat#226008, RRID: AB_2891278, 1:600), rat anti-HA (Roche, Cat# 11867423001, RRID: AB_390918, 1:100), donkey anti-rabbit Alexa Fluor 647 (Thermo Fisher Scientific, Cat# A-31573, RRID: AB_2536183, 1:1000), donkey anti-rat Alexa Fluor 488 (Thermo Fisher Scientific, Cat# A-21208, RRID: AB_2535794, 1:1000),chicken anti-Tyrosine Hydroxylase (anti-TH, Millipore, Cat# AB9702, RRID:AB_570923, 1:500), rabbit anti-TPH2 (Abcam, Cat# ab184505, RRID:AB_2892828, 1:500),goat anti-chicken Alexa Fluor 488 (Thermo Fisher Scientific, Cat# A32931, RRID:AB_2762843, 1:1000), goat anti-chicken Alexa Fluor 555 (Thermo Fisher Scientific, Cat# A32932, RRID:AB_2762844, 1:1000), donkey anti-rabbit Alexa Fluor 488 (Thermo Fisher Scientific, Cat# A21206, RRID:AB_2535792, 1:1000), donkey anti-rabbit Alexa Fluor 594 (Thermo Fisher Scientific, Cat# A21207, RRID:AB_141637, 1:1000), F(ab')2-Goat anti-Rabbit IgG (H+L) Secondary Antibody, FITC (Thermo Fisher Scientific, Cat# 11-4839-81, RRID:AB_1210845, 1:300)

Validation

rabbit anti-DOPA Decarboxylase was validated by the company and other groups:https://www.abcam.cn/products/primary-antibodies/dopa-decarboxylaseddc-antibody-ab3905.html.
rabbit anti-Fos was validated by the company and other groups: https://www.sysy.com/product/226008.
rat anti-HA was validated by the company and other groups: https://www.sigmaaldrich.cn/CN/zh/product/roche/roahaha.
donkey anti-rabbit Alexa Fluor 647 was validated by the company and other groups: https://www.thermofisher.cn/cn/zh/antibody/product/Donkey-anti-Rabbit-IgG-H-L-Highly-Cross-Adsorbed-Secondary-Antibody-Polyclonal/A-31573.
donkey anti-rat Alexa Fluor 488 was validated by the company and other groups: https://www.thermofisher.cn/cn/zh/antibody/product/Donkey-anti-Rat-IgG-H-L-Highly-Cross-Adsorbed-Secondary-Antibody-Polyclonal/A-21208.
chicken anti-Tyrosine Hydroxylase was validated by the company and other groups: https://www.sigmaaldrich.cn/CN/zh/product/mm/ab9702?msockid=1b668958eae867243c389c83eb8e66b8.
rabbit anti-TPH2 was validated by the company and other groups: https://www.abcam.com/en-us/products/primary-antibodies/tph2-antibody-epr19191-ab184505.
goat anti-chicken Alexa Fluor 488 was validated by the company and other groups: https://www.thermofisher.cn/cn/zh/antibody/product/Goat-anti-Chicken-IgY-H-L-Cross-Adsorbed-Secondary-Antibody-Polyclonal/A32931.
goat anti-chicken Alexa Fluor 555 was validated by the company and other groups: https://www.thermofisher.cn/cn/zh/antibody/product/Goat-anti-Chicken-IgY-H-L-Cross-Adsorbed-Secondary-Antibody-Polyclonal/A32932.
donkey anti-rabbit Alexa Fluor 488 was validated by the company and other groups: https://www.thermofisher.cn/cn/zh/antibody/product/Donkey-anti-Rabbit-IgG-H-L-Highly-Cross-Adsorbed-Secondary-Antibody-Polyclonal/A-21206.
donkey anti-rabbit Alexa Fluor 594 was validated by the company and other groups: https://www.thermofisher.cn/cn/zh/antibody/product/Donkey-anti-Rabbit-IgG-H-L-Highly-Cross-Adsorbed-Secondary-Antibody-Polyclonal/A-21207.
F(ab')2-Goat anti-Rabbit IgG (H+L) Secondary Antibody, FITC was validated by the company and other groups: https://www.thermofisher.cn/cn/zh/antibody/product/Goat-anti-Rabbit-IgG-H-L-Secondary-Antibody-Polyclonal/11-4839-81.

Eukaryotic cell lines

Policy information about cell lines and Sex and Gender in Research

Cell line source(s)	The CHO K1 cell line was obtained from ATCC (CCL-61).
Authentication	The CHO K1 cell line was authenticated using short tandem repeat (STR) profiling.
Mycoplasma contamination	All cell lines tested negative for mycoplasma contamination.
Commonly misidentified lines (See ICLAC register)	N/A

Animals and other research organisms

Policy information about studies involving animals; ARRIVE guidelines recommended for reporting animal research, and Sex and Gender in Research

Laboratory animals

C57BL/6J mice were purchased from Shanghai Laboratory Animal Research Center. Gpr139-Cre mice were generated using CRISPR/Cas9 based technology by Biocytogen (Beijing, China). Sert-Cre (B6.129(Cg)-Slc6a4tm1(cre)Xz/J, RRID: IMSR_JAX:014554), Th-Cre (B6.Cg-7630403G23RikTg(Th-cre)1Tmd/J, RRID:IMSR_JAX:008601), DAT-Cre (B6.SJL-Slc6a3tm1.1(cre)Bkmn/J, RRID:IMSR_JAX:006660), Vglut2-Cre (STOCK Slc17a6tm2(cre)Lowl/J, RRID:IMSR_JAX:016963) and Gad2-Cre (STOCK Gad2tm2(cre)Zjh/J; RRID:IMSR_JAX:010802) mice are obtained from the Jackson Laboratory. Gal-Cre mice (STOCK Tg(Gal-cre)KI87Gsat/Mmucd, RRID:

	MMRRC 031060-UCD) are obtained from Mutant Mouse Resource & Research Centers. Bama miniature pigs (Sus scrofa domestica) were purchased from LenSci (Suzhou, China).
Wild animals	No wild animals were used in this study.
Reporting on sex	Adult mice (>8 weeks old) of both sexes were used for experiments. We obtained similar experimental results from both sexes and pooled the data. All Bama miniature pigs were female adult.
Field-collected samples	No field-collected samples were used in this study.
Ethics oversight	All animal experiments were performed in accordance with NIH guidelines and approved by Animal Care and Use Committee of the Center for Excellence in Brain Science & Intelligence Technology, Chinese Academy of Sciences, Shanghai, China.

Note that full information on the approval of the study protocol must also be provided in the manuscript.

Plants

Seed stocks	N/A
Novel plant genotypes	N/A
Authentication	N/A